ACS OMEGA

http://pubs.acs.org/journal/acsodf

Article

Multicomponent Composite Membrane with Three-Phase Interface Heterostructure as Photocatalyst for Organic Dye Removal

Li Liu, Doudou Wang, Jun Huang, Zhixuan Huang, Ye Zhang, and Lili Li*

Cite This: *ACS Omega* 2022, 7, 17128−17143

Read Online

ACCESS | Metrics & More | Article Recommendations | Supporting Information

ABSTRACT: A multicomponent composite membrane (P-S-T/C) with three-phase interface heterostructure is ingeniously designed. A polydopamine (PDA)-modified conductive carbon fiber cloth (C_{FC}) is used as the substrate. Activated poly(vinylidene fluoride) (PVDF) with titanium dioxide (TiO_2) and a silicon dioxide (SiO_2) aerogel are electrospun as the top layer. The three-phase interface heterostructure was formed by TiO_2, conductive C_{FC}, and the SiO_2 aerogel. Its photocatalytic performance is validated by photodegradation of organic dyes in a low-oxygen (O_2) water environment. On combining with the capillary condensation of a bilayer structure, P-S-T/C exhibits excellent removal capability for anionic and cationic dyes. Moreover, P-S-T/C exhibits excellent stability and recyclability under simulated sunlight. The mechanism study indicates that the separated photogenerated carriers diffuse to the composite membrane surface rapidly on the three-phase interface of P-S-T/C. The abundant O_2 adsorbed on the porous SiO_2 aerogel surface acts as an electron (e^-)-trapping agent, which can also decrease the work function of the composite materials. Superoxide radicals ($^{\bullet}O_2^-$) play a dominant role in the reaction of photodegradation supported by a free radical-trapping experiment. This work paves a way to design a membrane with photocatalytic performance by constructing the interface heterostructure.

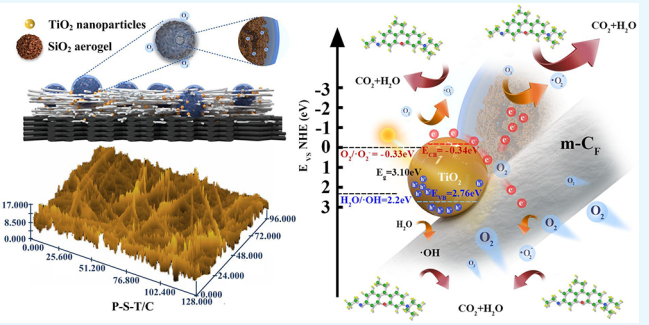

1. INTRODUCTION

Consumption of clean energy and water is a major obstacle for the sustainable development of the human society nowadays. Organic dyes are one of the major sources of water pollution. Synthetic organic dyes with aromatic ring structure and xenobiotic properties are noxious, highly carcinogenic, and nonbiodegradable. These dyes are widely used in paper, textile, pulp, dyeing, and other industries, and consequently cause serious threats to the ecosystem.[1−3] Conventional approaches such as biological processes, advanced oxidation processes, reverse osmosis, and electrochemical coagulation have been employed to handle the issue of dye contamination. Nevertheless, these approaches still have some disadvantages, including incomplete degradation, high consumption, complex operation, and strict reaction conditions.[4]

Photocatalysis has been used in many fields like photocatalytic reduction of CO_2,[5−7] photocatalytic hydrolysis for hydrogen production,[8−10] and photocatalytic degradation of organic pollutants[11,12] due to its merits of simple operation, strong oxidation ability, and avoidance of secondary pollution.[13−15] Huang et al.[8] synthesized copper nanoparticles on graphene nanosheets (Cu/graphene) in vacuum; the photocatalytic hydrogen evolution rate of Cu/graphene was 3.2 times that of pure Cu NPs. Anatase TiO_2, as a semiconductor photocatalyst,[16,17] has been attracting wide attention due to its potential application in solar energy storage and conversion.[18−20] In most reported research works, the photocatalytic performance of the TiO_2 photocatalyst was improved via photogenerated carriers separated at a low band gap rapidly. A range of strategies have been used, such as charge separation, light absorption, and the active surface of TiO_2.[21] Meng et al.[22] prepared the $TiO_2/Ni(OH)_2$ composite photocatalyst via a simple wet chemical precipitation method, which displayed remarkably boosted photocatalytic CO_2 reduction activity due to the formation of a semiconductor heterostructure. Yu et al.[23] fabricated a hybrid $TiO_2/SiO_2/g\text{-}C_3N_4$ composite photocatalyst with superstructure (UTSCN) via the soft-template method, which exhibited the enhanced synergistic effects of adsorption and photodegradation. Compositing with two-dimensional carbon materials to enhance the electronic conductivity is also an efficient avenue to ameliorate the photocatalytic properties of TiO_2. Then, e^- trapping agents are added to restrain the recombination of e^-−h^+ pairs. But the optimal photocatalytic performance cannot be

Received: February 2, 2022
Accepted: March 21, 2022
Published: May 15, 2022

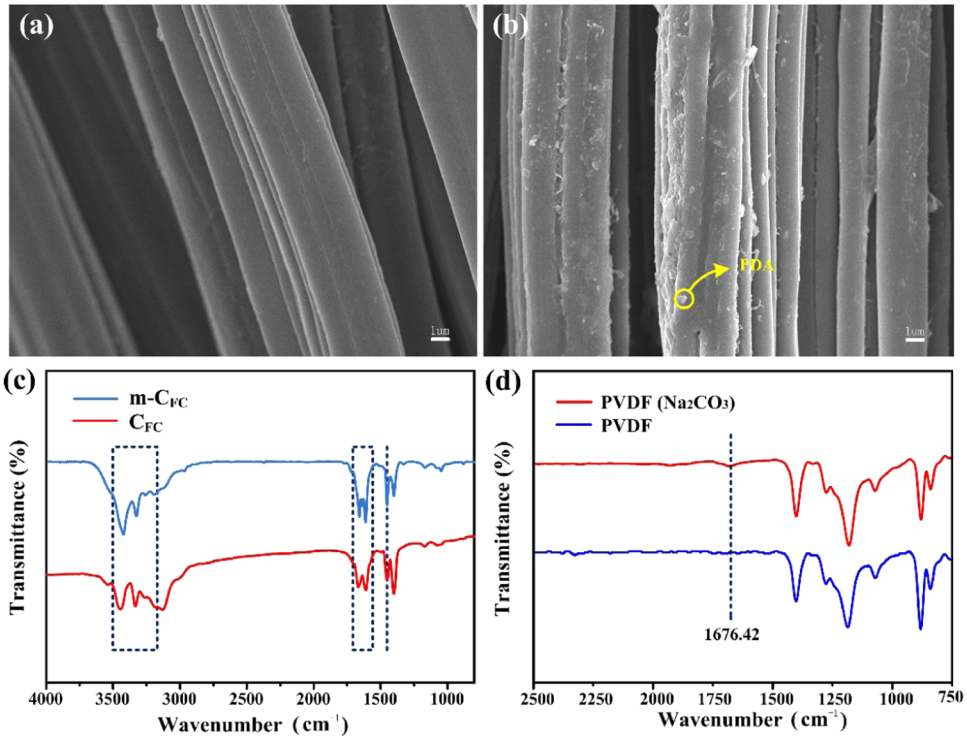

Figure 1. SEM images of the C_{FC} substrate (a) before and (b) after modification. (c) FTIR spectra of the C_{FC} substrate before and after modification with PDA. (d) FTIR spectra of pristine PVDF powder before and after activation in carbonate buffer.

achieved because the trapped e^- is exhausted and only h^+ plays a dominant role in the photocatalytic reaction.[24] Work function is the energy required for transferring an e^- from the material's surface, which is regulated by the surface defects, ambient gases (such as O_2), and types of materials.[25] There are some interesting research works suggesting that the work function of materials will affect their photocatalytic performance.[26,27] However, most photodegradation occurs in the low-O_2 environment of the aqueous solution, which will decrease the photocatalytic performance. If O_2 adsorbed on the materials surface is used as an e^- trapping agent to produce $^{\bullet}O_2^-$ for photodegradation (one of the reaction paths of photocatalysis), the work function of the materials may be reduced, e^- and h^+ can also be fully utilized in the photocatalytic process.

The combination of photocatalysis and adsorption is also an effective method to improve the removal performance of organic dyes. Chen et al.[28] presented a new and effective strategy to synthesize a ZnO@C-N-Co core−shell nanocomposite, which showed excellent synergistic adsorption/photodegradation of organic pollutants. Wang et al.[29] synthesized $BiVO_4$/carbon sphere nanocomposites, which showed excellent adsorption and photocatalytic performance for organic dyes. However, the optimally photocatalytic performance is restrained because of the exhaustion of trapped e^-. The stability and recyclability of composite photocatalysts needed to be further improved.

In this work, a dual-layer composite membrane with a three-phase interface heterostructure was fabricated. The top layer was the poly(vinylidene fluoride) (PVDF)/TiO_2 nanoparticles/SiO_2 aerogel electrospinning membrane. The carbon fiber cloth (C_{FC}) substrate and PVDF top-layer composite membrane were tightly bonded by active functional groups (such as amine groups, catechol groups, and aromatic moieties) in polydopamine (PDA).[30,31] The photocatalytic activity of the prepared composite membrane under simulated sunlight was studied in detail. The capillary condensation in P-S-T/C with dual-layer structure endowed its high adsorption capability. The heterostructure formed by TiO_2 nanoparticles and the C_{FC} substrate accelerated the diffusion of photogenerated carriers to the surface of the membrane. The SiO_2 aerogel could supply adsorbed O_2 molecules, which acted as an e^- trapping center to minimize carrier recombination. The work function of the composite materials was evaluated by ultraviolet photoelectronic spectrum (UPS).

2. RESULTS AND DISCUSSION

2.1. Preparation of the Dual-Layer Composite Membrane. *2.1.1. Modification of C_{FC} Substrate.* The surface morphologies of the C_{FC} substrate and m-C_{FC} substrate are shown in Figure 1a,b. After deposition of PDA, the surface changed from smooth (C_{FC}) to rough (m-C_{FC}). The FTIR spectra of C_{FC} and m-C_{FC} are illustrated in Figure 1c. Compared with C_{FC}, m-C_{FC} displayed several enhanced peaks. The peaks at 3500−3200 cm^{-1} are ascribed to the stretching vibration of the free amino and hydroxyl groups in PDA.[32] The peaks at 1647.97 and 1606.68 cm^{-1} are attributed to the C═C and N−H vibrations, respectively. The peak at 1450.45 cm^{-1} is assigned to the stretching vibrations of −C−N− in PDA.[33,34] These results suggested that PDA was synthesized on the surface of C_{FC}.

2.1.2. Top Layer of the Composite Membrane. The FTIR spectra of pristine PVDF powder and activated PVDF powder are illustrated in Figure 1d. The wavenumbers of pristine PVDF powder were assigned as follows: 1401.39 (scissoring of CH_2 groups), 1278.10 (CH_2 rocking), 1183.26 (CH_2/CH_3 deformation), 1069.46 (CF_2 symmetric stretching), and 841.84 cm^{-1} (rocking and asymmetric stretching of CH_2/CF_2).[35,36] In

https://doi.org/10.1021/acsomega.2c00686
ACS Omega 2022, 7, 17128−17143

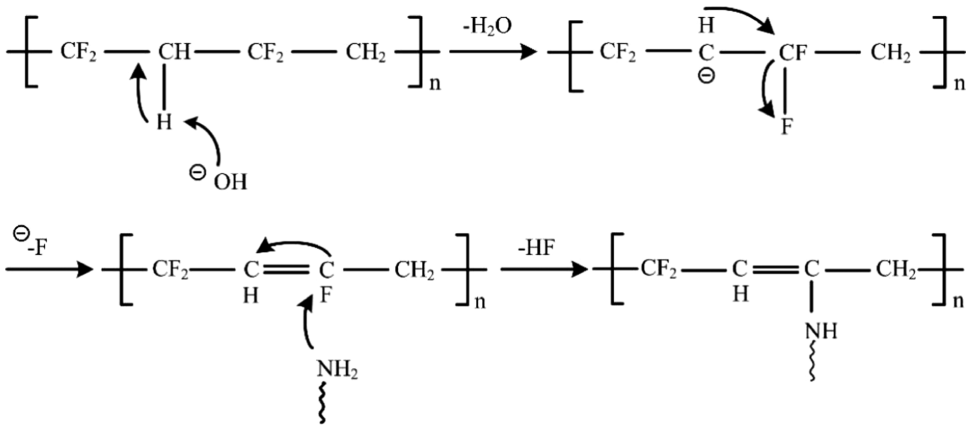

Figure 2. Activation process of PVDF in carbonate buffer.

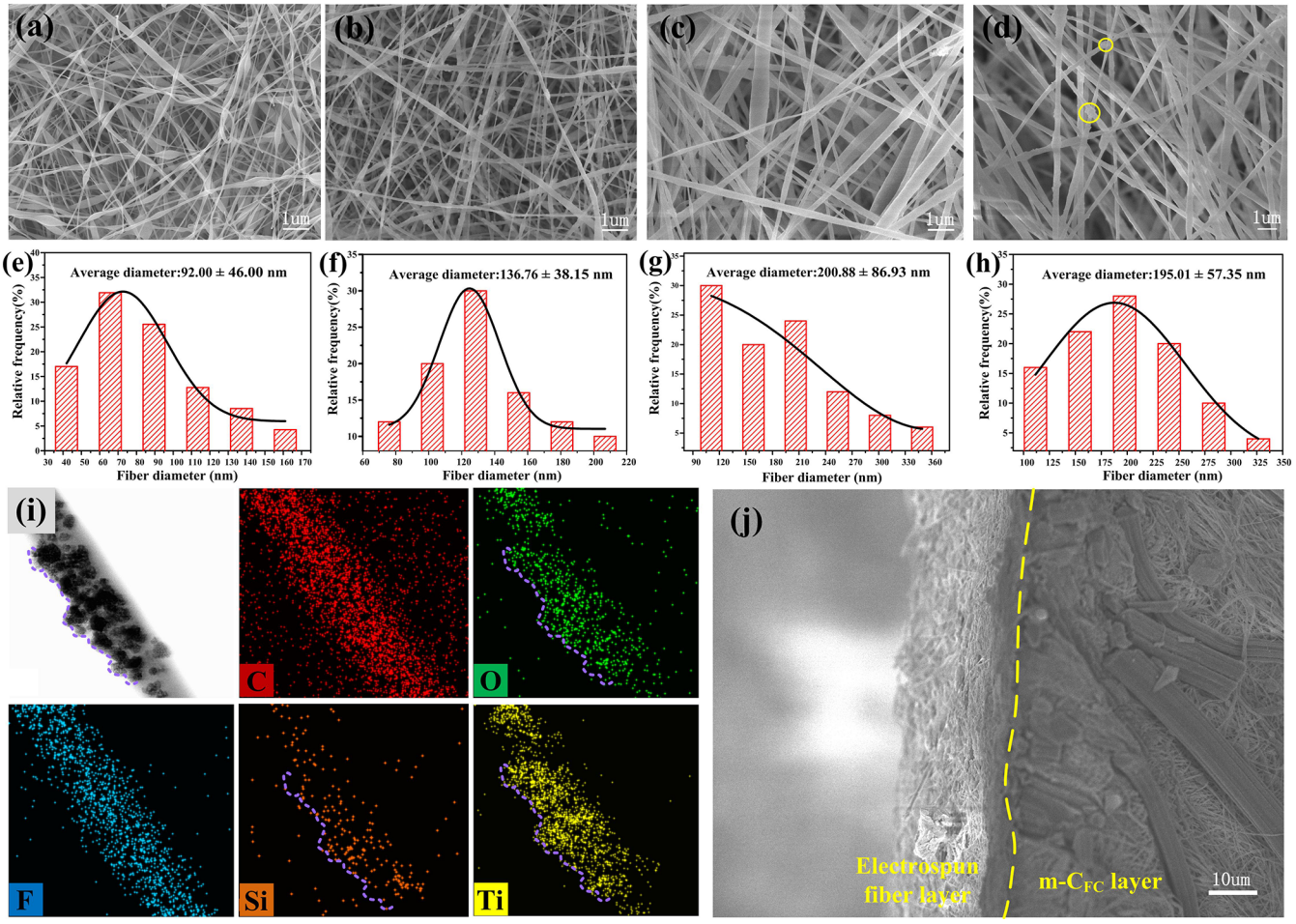

Figure 3. Top layer of the composite membrane: SEM images of (a) PVDF/C, (b) P-TiO_2/C, (c) P-SiO_2/C, and (d) P-S-T/C; the diameter distribution of (e) PVDF/C, (f) P-TiO_2/C, (g) P-SiO_2/C, and (h) P-S-T/C respectively. (i) TEM image of P-S-T/C and EDS elemental mapping of C, O, F, Si, and Ti. (j) SEM image of the cross section of P-S-T/C.

comparison to pristine PVDF powder, the enhanced peak at 1676.42 cm^{-1} is attributed to the C=C stretching vibration of the activated PVDF powder,[37] which proved that the active double bonds were formed during the activation process with carbonate buffer.

The proposed mechanism for PVDF activation is shown in Figure 2. The activated PVDF contained a double bond after elimination of HF.[38,39] The reaction for PVDF activation contained several stages. Under high-alkalinity and high-temperature conditions, the CH_2 group in the PVDF chain was deprotonated. The obtained anion was stabilized because of the presence of fluorine (four e^--withdrawing atoms). Then, F ions were the driving force for the formation of double bonds. Finally, the nucleophilic attack of amino groups on the modified C_{FC} substrate resulted in nucleophilic substitution of F in the sp^2-hybridized carbon.[40−42] The electrospun-activated PVDF fibers were used as the top layer on modified C_{FC} substrate.

https://doi.org/10.1021/acsomega.2c00686
ACS Omega 2022, 7, 17128−17143

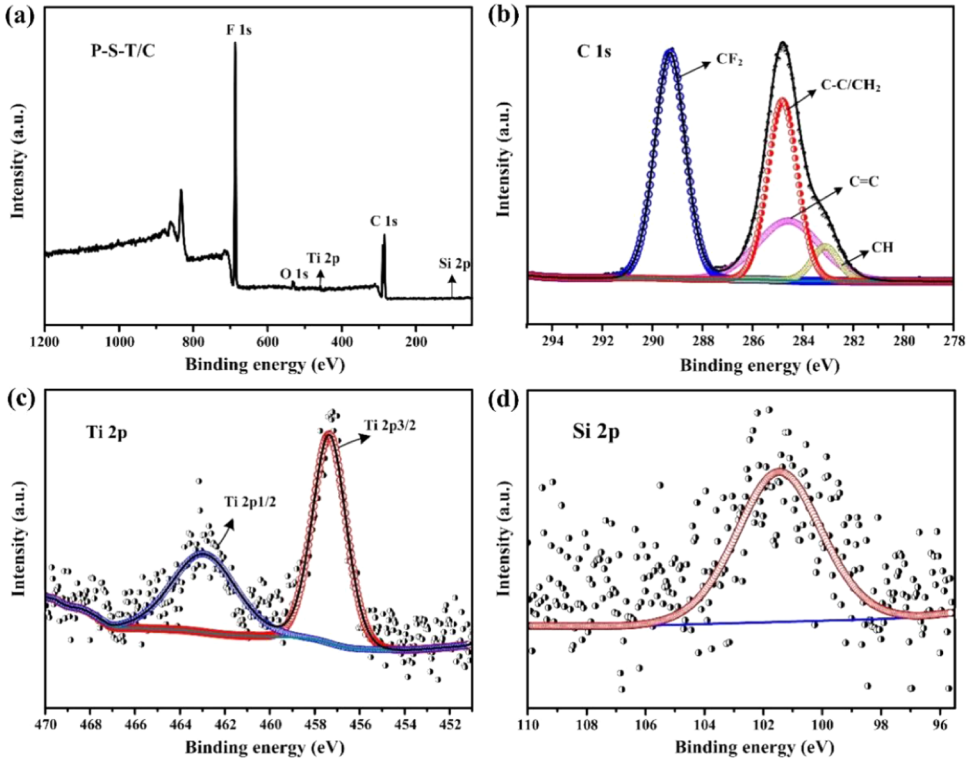

Figure 4. XPS of P-S-T/C: (a) full-spectra scanning and high-resolution spectra for (b) C 1s, (c) Ti 2p, and (d) Si 2p.

2.2. Structures of the Composite Membrane. *2.2.1. SEM and TEM Analysis.* The morphologies of all of the prepared top-layer membranes are depicted in Figure 3. The viscosity and conductivity of the precursor solutions are listed in Table S2. Figure 3a presents the top-layer morphology of PVDF/C. The membrane exhibited a fibrous nonwoven network with a fiber diameter of 92.00 ± 46.00 nm (Figure 3e). A large number of interconnecting pores and beaded structures on the fiber surface were observed. After the incorporation of TiO_2 nanoparticles into PVDF fibers (Figure 3b), the beaded structures decreased, but some knots could still be observed. The fiber diameter increased to 136.76 ± 38.15 nm (Figure 3f), which meant that viscosity contributed more to fiber diameter than conductivity in the precursor solution. In Figure 3c, after incorporation of the SiO_2 aerogel into PVDF fibers, the fiber diameter increased to 200.88 ± 86.93 nm (Figure 3g) and the beaded structures disappeared. This was ascribed to an increase in viscosity and decrease in electrical conductivity of the precursor solutions. In Figure 3d, the top-layer morphology of P-S-T/C also is seen to exhibit the porous nonwoven fabric network structure with a coarse surface. The average diameter of the fiber increased to 195.01 ± 57.35 nm (Figure 3h) in comparison to PVDF/C. It was the result of the synergistic effect of viscosity and conductivity on the precursor solutions.[43,44]

The TEM image and corresponding energy dispersive spectroscopy (EDS) elemental mapping of P-S-T/C are shown in Figure 3i. The TiO_2 nanoparticles and SiO_2 aerogel were evenly distributed through the nanofiber. The distributions of C and F elements were observed in a typical C and F mapping of the PVDF fibers. The distributions of O, Si, and Ti elements were the same as those in the TEM image, which further proved the uniform distribution of TiO_2 nanoparticles and the SiO_2 aerogel in PVDF fibers. The signal of Si elements was weaker than that of Ti elements because of the lesser amount of the SiO_2 aerogel than the TiO_2 nanoparticles in the precursor solution. Figure 3j reveals the cross section of the P-S-T/C dual-layer composite membrane. It is visible that the two layers could be tightly integrated.

2.2.2. XPS Analysis. XPS technique was carried out to determine the surface chemical composition within 10 nm of the composite membrane. Figure 4a shows the XPS survey scan spectra of P-S-T/C, in which O (1s), C (1s), Si (2p), Ti (2p), and F (1s) elements were identified. The high intense peak of F was attributed to the high content of F in PVDF. The low intense peaks of Ti and Si were attributed to their relatively low contents compared to PVDF. Figure 4b illustrates the main C 1s peak at 285.0 eV. The peak at 284.6 eV corresponded to the C═C of activated PVDF,[45] and the peaks centered at 289.2, 284.8, and 283.1 eV were attributed to $-CF_2$, $C-C/CH_2$, and CH, respectively.[46] Figure 4c presents the Ti 2p high-resolution XPS spectra. The peaks at 464.0 and 458.0 eV corresponded to the Ti_4^+ $2p_{1/2}$ and Ti_4^+ $2p_{3/2}$ spin−orbital splitting photoelectrons at around 5.6 eV, respectively, suggesting that the Ti elements existed as the Ti_4^+ state.[47,48] Figure 4d shows the high-resolution XPS spectra of Si 2p. The peak at 101.5 eV was attributed to the Si(IV) chemical state,[49] implying that the SiO_2 aerogel was on the surface of P-S-T/C.

The theoretical and experimental values of the surface atomic compositions in these samples were calculated as shown in Table S3. The Si element content on the surface of P-SiO_2/C calculated by XPS was 4.34%, which matched well with the theoretical added Si content in P-SiO_2/C (4.24%). This indicated that SiO_2 aerogel was dispersed evenly in the PVDF fibers. The Ti element content (1.69%) on the surface of P-TiO_2/C was much lower than its theoretical added content in P-TiO_2/C (13.85%); this was because the

https://doi.org/10.1021/acsomega.2c00686
ACS Omega 2022, 7, 17128−17143

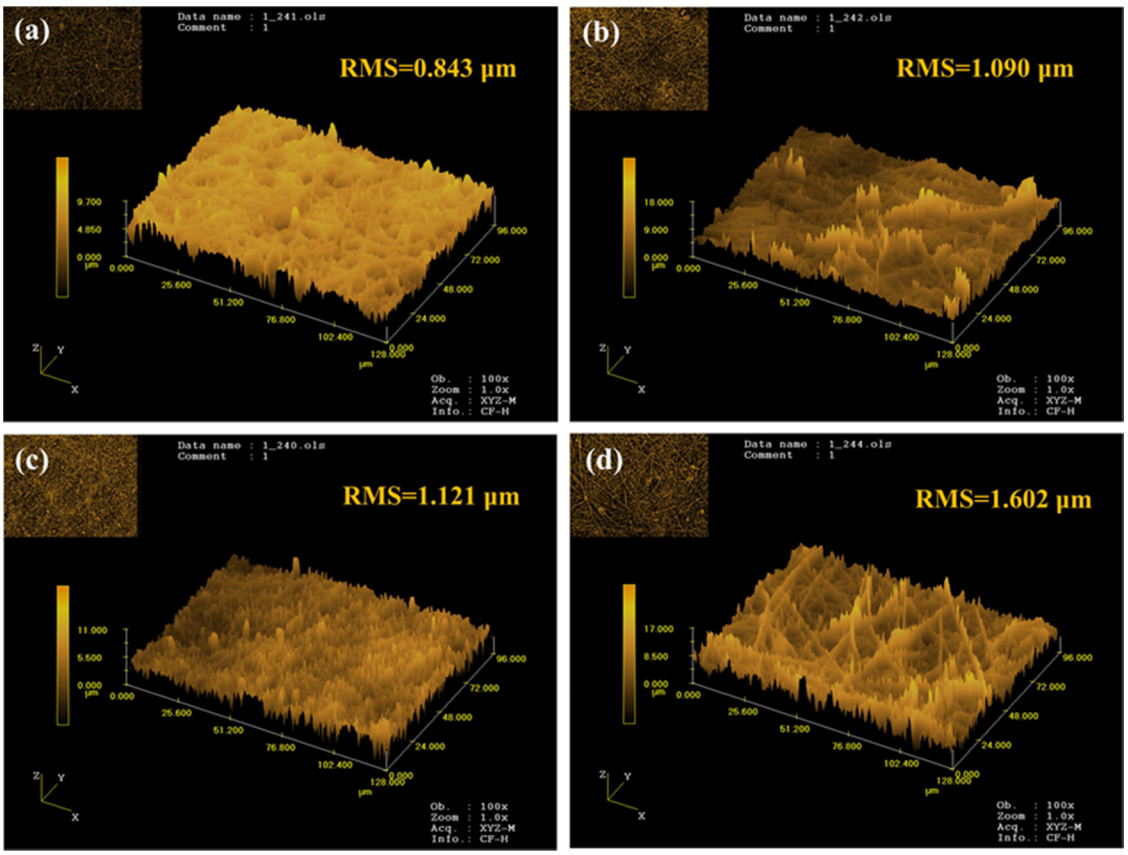

Figure 5. LSCM images of the top-layer membranes of (a) PVDF/C, (b) P-SiO_2/C, (c) P-TiO_2/C, and (d) P-S-T/C.

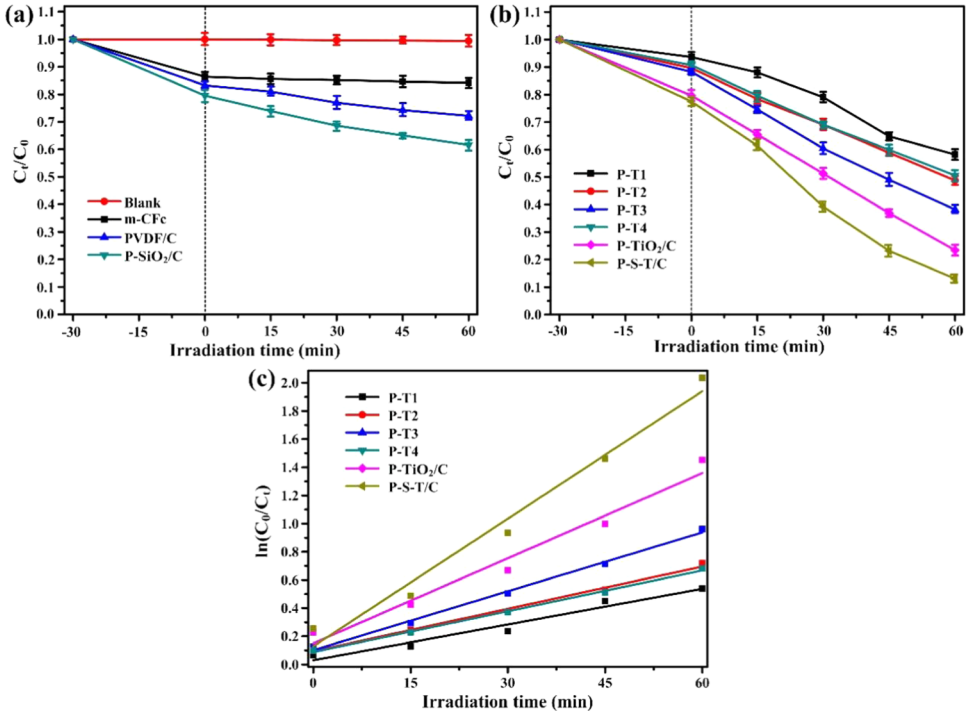

Figure 6. (a, b) Photodegradation of RhB with different membranes and (c) the corresponding reaction rate plots [reaction conditions: initial concentration = 12 mg L^{-1}, photocatalyst = 0.4 g, pH = 6.0, simulated sunlight irradiation].

semiconductor TiO_2 nanoparticles tended to disperse near the conductive C_{FC} substrate. For P-S-T/C, when the SiO_2 aerogel and TiO_2 nanoparticles were added simultaneously, the Ti element content on the surface (1.96%) was still lower than its theoretical content in P-TiO_2/C (12.86%). The content of the SiO_2 aerogel (5.59%) on the surface of P-S-T/C was much

https://doi.org/10.1021/acsomega.2c00686
ACS Omega 2022, 7, 17128−17143

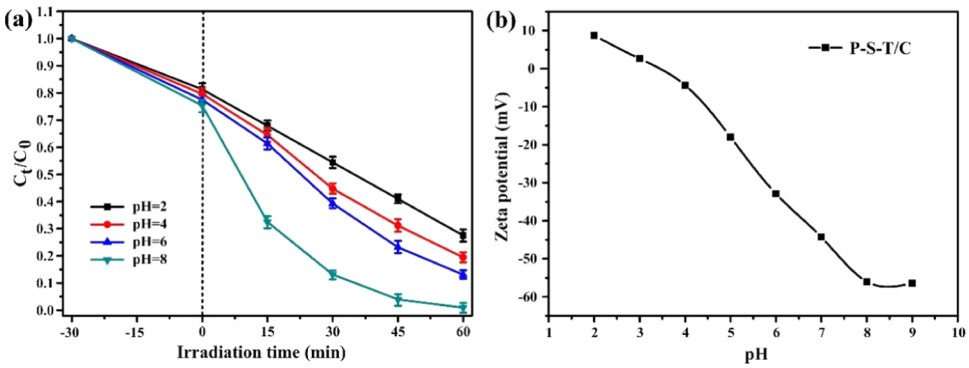

Figure 7. (a) Photodegradation rates of RhB by P-S-T/C at different pH values [reaction conditions: initial concentration = 12 mg L^{-1}, photocatalyst = 0.4 g, pH = 2.0, 4.0, 6.0, and 8.0, simulated sunlight irradiation]. (b) Dependence of the ζ-potential of the P-S-T/C membrane surface on pH values.

higher than its theoretical added content in P-S-T/C (3.33%), confirming that the SiO_2 aerogel tended to disperse on the surface of the fibers.

2.2.3. Roughness Analysis. Figure 5 shows the two-dimensional (inset) and three-dimensional LSCM images of all of the prepared top-layer membranes. These two-dimensional images indicated that all top-layer membranes exhibited the fibrous nonwoven network, matching well with the SEM analysis (Figure 3). The topographies of the membrane surfaces were characterized by root-mean-square (RMS) roughness, which represented the average height fluctuation across the entire LSCM scan size.[50] Figure 5a shows the three-dimensional LSCM image of PVDF/C with an RMS roughness of ca. 0.843 μm. Compared with PVDF/C, the RMS roughness slightly increased to ca. 1.090 μm for P-SiO_2/C (Figure 5b) and to ca. 1.121 μm for P-TiO_2/C (Figure 5c). The simultaneous addition of SiO_2 aerogel and TiO_2 nanoparticles (Figure 5d) would greatly increase the RMS roughness to ca. 1.602 μm. The three-dimensional porous network architecture could be observed obviously, which was consistent with the surface morphology of the SiO_2 aerogel in Figure S1. The distributions of the SiO_2 aerogel and TiO_2 nanoparticles observed by LSCM were in accordance with the results obtained by XPS analysis.

2.3. Evaluation of Organic Dye Removal Performance. *2.3.1. Removal Performance of RhB.* The effects of different components in the composite membrane on the removal of RhB were investigated in detail. The degradation rates are summarized in Table S4. As shown in Figure 6a,b, the C_{FC} substrate could adsorb 13.64% of the RhB under dark conditions within 30 min, while the PVDF/TiO_2 single-layer membrane could barely adsorb RhB. After combining with the C_{FC} substrate, the adsorption rate of the PVDF/C dual-layer composite membrane increased to 16.73%, indicating that the capillary condensation by the dual-layer architecture promoted the RhB adsorption capability. After adding the SiO_2 aerogel, the adsorption rate of the P-SiO_2/C composite membrane continually increased to 20.46%. It was because more adsorption space for organic dyes was provided by the addition of the SiO_2 aerogel.

Figure S2 depicts the curves of RhB removal by P-SiO_2/C with and without light within 90 min. No significant difference in removal efficiency was observed, indicating that the components for PVDF, SiO_2, and the C_{FC} substrate had no photocatalytic performance. For the PVDF/TiO_2 single-layer membrane, the photodegradation rate gradually increased with the increase of TiO_2 contents. When the TiO_2 contents reached 3% (w/v), the degradation rate of RhB reached 61.78% within 60 min of simulated sunlight irradiation. With further increase of TiO_2 contents, the photodegradation rate declined (Figure 6b). After combining with the C_{FC} substrate, the P-TiO_2/C dual-layer composite membrane could remove 76.61% of RhB within 60 min of simulated sunlight irradiation. The photocatalytic performance improved because the e^- conduction rate was accelerated by the interface bonding between the C_{FC} substrate and TiO_2 nanoparticles. The RhB removal rate of P-S-T/C further increased to 86.92% within 60 min. This indicated that the photocatalysis was enhanced by the composition of the SiO_2 aerogel, TiO_2 nanoparticles, and C_{FC} substrate.

The photodegradation kinetics study for the composite membrane were assumed to be identified with the Langmuir–Hinshelwood (L–H) model and expressed as eq 1[51]

$$r = -\frac{dC}{dt} = \frac{kKC}{1 + KC} \quad (1)$$

where r is the degradation rate, C (mg L^{-1}) is the concentration of RhB, t (min) is the running time of the simulated sunlight irradiation, k (mg L^{-1} min^{-1}) is the reaction rate constant, and K (L mg^{-1}) is the equilibrium constant. The term kK could be regarded as an apparent rate constant k_{app} (min^{-1}). Therefore, eq 1 was expressed as eq 2

$$r = -\frac{dC}{dt} = \frac{k_{app}C}{1 + KC} \quad (2)$$

where $KC \ll 1$ in lower-concentration solutions of RhB. The above equation could be reduced to the first-order equation and expressed as eq 3

$$r = -\frac{dC}{dt} = k_{app}C \quad (3)$$

To confirm the above assumption, the curve of $\ln(C_0/C_t)$ vs t and the kinetics constants are shown in Figure 6c and Table S4, respectively. The linear relations of $\ln(C_0/C_t)$ and t were validated. The determined coefficients (R^2) were all greater than 0.95, confirming that the photodegradation kinetics fitted well with the pseudo-first-order kinetic model. The k_{app} values of P-T3, P-TiO_2/C, and P-S-T/C were 0.0140, 0.0202, and 0.0302 min^{-1}, respectively. The maximum k_{app} value of P-S-T/C indicated the best photocatalytic performance.

https://doi.org/10.1021/acsomega.2c00686
ACS Omega 2022, 7, 17128−17143

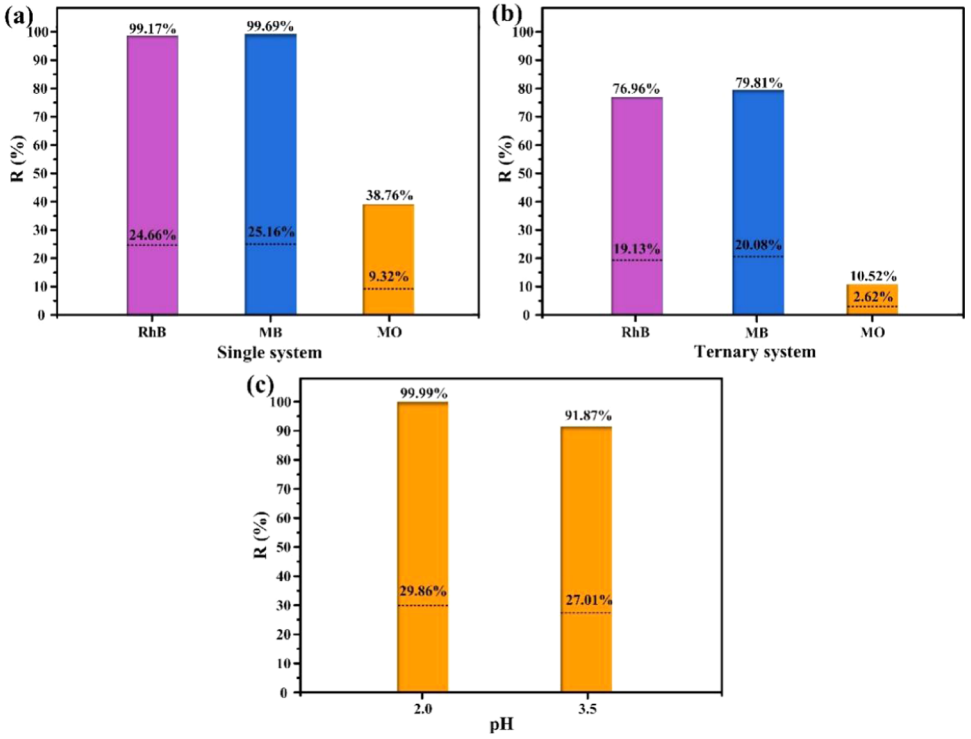

Figure 8. Different dye removal rates of the P-S-T/C dual-layer composite membrane in a (a) single and (b) ternary system [reaction conditions: initial concentration = 12 mg L^{-1}, photocatalyst = 0.4 g, pH = 8.0, simulated sunlight irradiation]. (c) Removal rates of MO at pH 2.0 and 3.5 [reaction conditions: initial concentration = 12 mg L^{-1}, photocatalyst = 0.4 g, simulated sunlight irradiation].

2.3.2. Impact of pH on RhB Removal Performance. The influence of pH on RhB removal by P-S-T/C is displayed in Figure 7a. P-S-T/C could remove 72.48% of the RhB cationic dye within 60 min at pH 2.0. The RhB removal rate increased with increasing pH of the dye solutions, and the maximum removal rate of 99.17% appeared at pH 8.0 within 60 min. The ζ-potential of the composite membrane surface was observed under the different pH values. As presented in Figure 7b, the P-S-T/C membrane had an isoelectric point at pH = 3.5 (pH_{pzc}-3.5).[52] At pH < pH_{pzc}, the P-S-T/C membrane was positively charged, and the electrostatic repulsion between the membrane and RhB cationic dyes caused the decrease in removal rate. At pH > pH_{pzc}, the P-S-T/C membrane was negatively charged, and the electrostatic attraction between the membrane and RhB cationic dyes promoted the RhB removal rate. The electrostatic attraction interactions gradually increased with the increase of pH, and reached the maximum removal rate of RhB at pH = 8.0.

The kinetics plots of P-S-T/C at different pH values are investigated in Figure S3; the reaction kinetic constant reached 0.0726 min^{-1} at pH = 8.0, which further proved that the P-S-T/C composite membrane had excellent removal efficiency for RhB under alkaline conditions.

2.3.3. Selective Competitive Removal of Organic Dyes. The removal rates of the P-S-T/C dual-layer composite membrane for RhB and MB (cationic dyes) and MO (anionic dyes) were compared at the same concentrations and at a pH value of 8.0. As shown in Figure 8a, the adsorption capability in a single organic dye without light was in the following order: MB > RhB > MO. After 60 min of simulated sunlight irradiation, the removal rates for 99.17% RhB, 99.69% MB, and 38.76% MO by P-S-T/C were achieved.

The selective synergistic adsorption/photodegradation behavior of the composite membrane in the ternary system of RhB, MB, and MO was studied. P-S-T/C weighing 0.4 g was added to 60 mL (4 mg L^{-1} RhB, 4 mg L^{-1} MB and 4 mg L^{-1} MO) of mixed solution, and the removal rates in the ternary organic dye system for P-S-T/C were tested. As shown in Figure 8b, the negatively charged P-S-T/C showed higher removal rates for the cationic dyes at pH = 8.0, implying that P-S-T/C could provide selective removal of cationic dyes.

According to the above analysis, the P-S-T/C composite membrane showed excellent removal capability for cationic dyes when the pH value was greater than pH_{pzc}. Then, the pH value of the MO solution was set at 2.0 and 3.5 (pH_{pzc}) to further investigate the removal capability of P-S-T/C for anionic dyes. As shown in Figure 8c, after 60 min of simulated sunlight irradiation, P-S-T/C could remove 91.37% of the MO at pH = 3.5. At pH = 2.0, the removal rate for MO was more than 99.99%, which was higher than that of RhB (72.48%) under the same conditions. Therefore, when the pH value of the organic dye aqueous solution was greater than pH_{pzc}, the negatively charged P-S-T/C surface favored adsorbtion of positive cationic dyes. When the pH value was lower than pH_{pzc}, positively charged P-S-T/C could almost completely remove anionic dyes. Compared with the reported photocatalysts in other researches, P-S-T/C showed excellent photocatalytic performance for all types of organic dyes (Table S5).[53−59]

2.3.4. Impact of RhB Initial Concentration on Its Removal Performance. Figure S4 describes the influence of the RhB initial concentration on the removal rate of P-S-T/C. The removal rate of P-S-T/C decreased with increasing concentration of the RhB. At a lower initial concentration, P-S-T/C provided sufficient reactive active sites for RhB. With the

https://doi.org/10.1021/acsomega.2c00686
ACS Omega 2022, 7, 17128−17143

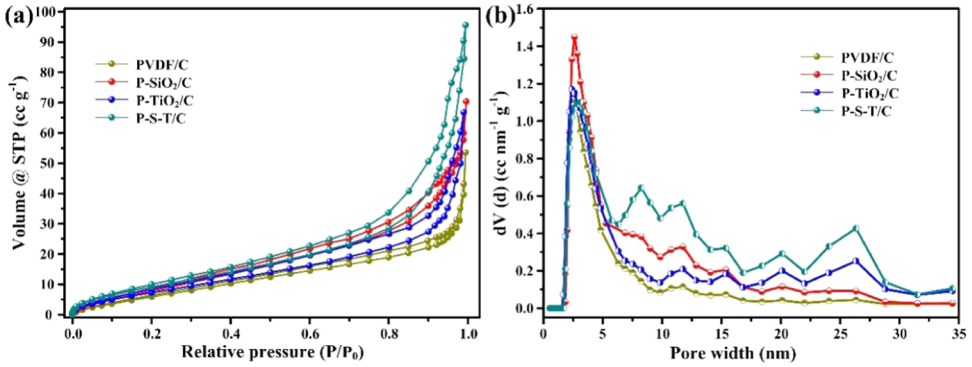

Figure 9. (a) N_2 adsorption−desorption isotherms of the top-layer membrane and (b) their corresponding BJH pore-size distribution plots.

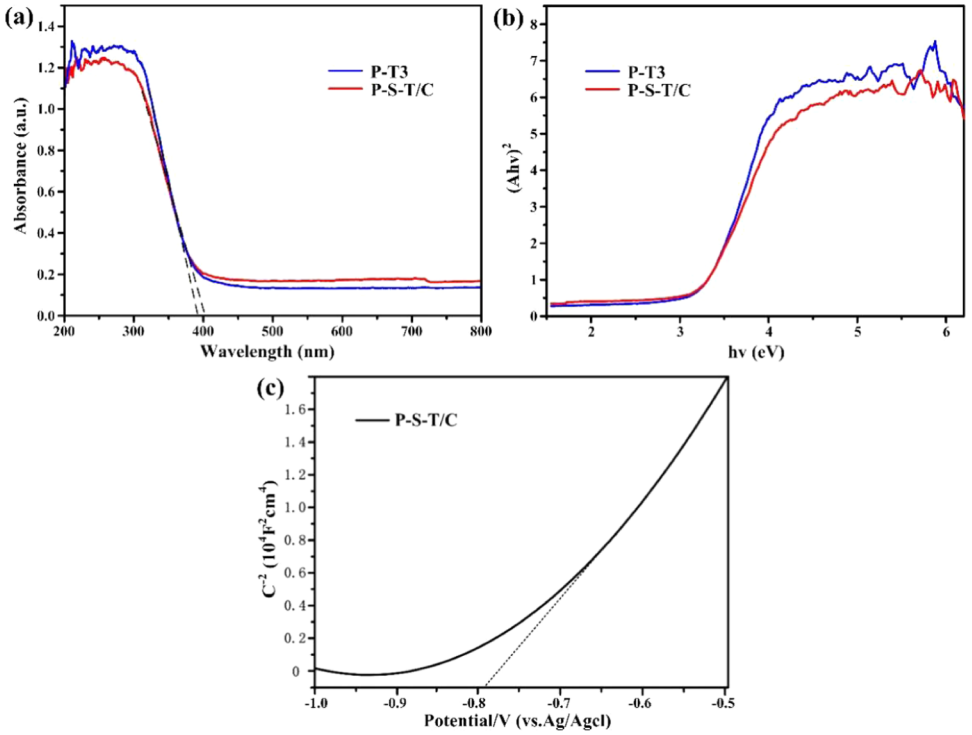

Figure 10. (a) UV−vis DRS and (b) corresponding plots of $(\alpha h\nu)^2$ vs $(h\nu)$ for calculating the E_g of P-T3 and P-S-T/C; (c) Mott−Schottky plot of P-S-T/C.

increase of the initial concentration, more RhB would compete for the reactive active sites. In addition, as the initial RhB concentration increased, more RhB molecules were adsorbed onto the P-S-T/C surface. The RhB molecules also absorbed light, which affected the arrival of light to the surface of the P-S-T/C, thus reducing the efficiency of photocatalytic degradation.[60]

2.4. Mechanism Analysis of RhB Removal. *2.4.1. Brunauer−Emmett−Teller (BET) Analysis of the Top-Layer Membrane.* The porosity and specific surface area (S_{BET}) of the top-layer membrane were investigated by nitrogen (N_2) adsorption−desorption isotherms. As shown in Figure 9a, all of these curves exhibited type IV isotherms. In comparison to the PVDF matrix membrane, P-SiO_2/C, P-TiO_2/C, and P-S-T/C exhibited typically a H3-type hysteresis loop. Especially for P-S-T/C, the hysteresis loop had a larger closed area because of the capillary condensation both in the architecture of the dual layer and in the mesoporous region formed by the accumulation of micro/nanoparticles on the membrane surface.[61,62] The N_2 adsorption capacities of the different composite membranes were as follows: PVDF/C < P-TiO_2/C < P-SiO_2/C < P-S-T/C. The P-S-T/C composite membrane exhibited the best N_2 adsorption capacity.

The Barrett−Joyner−Halenda (BJH) pore-size distributions of PVDF/C, P-TiO_2/C, P-SiO_2/C, and P-S-T/C are shown in Figure 9b. The PVDF matrix membrane exhibited uniform pores, which were concentrated at about 3 nm. P-SiO_2/C and P-TiO_2/C exhibited different distributions of hierarchical pore structure. P-S-T/C had the most obvious hierarchical pore structure. It was attributed to the aggregations of the SiO_2 aerogel and TiO_2 nanoparticles. The above analysis further clarified the improved roughness, which agreed with the LSCM results. The hierarchical pore structure would provide efficient transport pathways for the dye molecules in photodegradation.[63] In addition, the S_{BET} and pore volume of P-S-T/C increased in comparison to the PVDF matrix membrane, as seen in Table S6. It was due to the formation of the three-dimensional porous network structure, which could provide

https://doi.org/10.1021/acsomega.2c00686
ACS Omega 2022, 7, 17128−17143

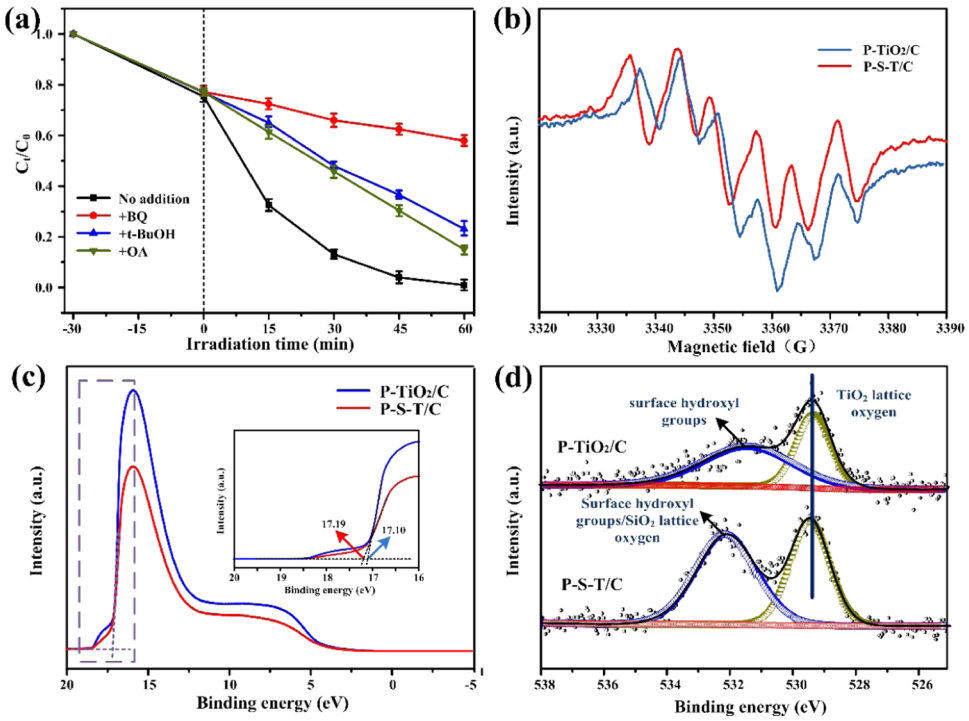

Figure 11. (a) Evolution of the photocatalytic activity of P-S-T/C in the presence of different scavengers for the degradation of RhB [initial concentration = 12 mg L^{-1}, photocatalyst = 0.4 g, pH = 8.0, simulated sunlight irradiation]. (b) EPR spectra of P-TiO_2/C and P-S-T/C for DMPO−$^{\bullet}O_2^-$ formed in irradiated methanol dispersion. (c) UPS spectra of P-TiO_2/C and P-S-T/C. (d) High-resolution XPS O 1s spectra of P-TiO_2/C and P-S-T/C.

more active adsorption sites and sufficient adsorption space for organic dyes.

2.4.2. Optical and Electrochemical Characterization. To compare the maximum light absorption wavelength and band structure of P-T3 and P-S-T/C, the UV−vis DRS test was performed. As shown in Figure 10a, P-S-T/C exhibited a wider light absorption range in comparison to P-T3. It was ascribed to the formation of the three-phase heterostructure between the TiO_2 nanoparticles, SiO_2 aerogel, and conductive C_{FC} substrate. Tauc plots were used to estimate the band structures of P-T3 and P-S-T/C (Figure 10b). The band-gap energy could be calculated by eq 4

$$\alpha h\nu = C(h\nu - E_g)^n \tag{4}$$

where α is the light absorption coefficient of the semiconductor, hν is the incident photon energy, C is the light speed, n is 2 for the n-type semiconductor and 1/2 for the p-type semiconductor, and E_g is the band-gap energy. According to the above equation, the calculated E_g values of P-T3 and P-S-T/C were 3.2 and 3.1 eV, respectively. The increase in light absorption range and the decrease in band-gap energy of P-S-T/C played a critical role in the improvement of photocatalytic performance.

To better understand the mechanism of interfacial charge separation and transfer, the Mott−Schottky test was conducted. Figure 10c displays the Mott−Schottky plot of P-S-T/C; the positive slope indicates its classic n-type conductive behavior. The flat band potential value (E_{fb}) acquired from the x-intercept was about −0.79 eV (vs Ag/AgCl reference). The value of E_{fb} (vs Ag/AgCl) could be converted to E_{RHE}, which is the converted potential vs the reversible hydrogen electrode (RHE), as shown in eq 5

$$E_{RHE} = E_{Ag/Agcl} + 0.059pH + E^0_{Ag/Agcl} \tag{5}$$

where $E_{Ag/AgCl}$ is the experimentally measured potential (vs Ag/AgCl reference), pH = 6, and $E_{Ag/AgCl}{}^0$ = 0.1976 at 25 °C. The E_{RHE} value of P-S-T/C was calculated to be −0.24 eV. For an n-type semiconductor, the conduction band energy (E_{CB}) is negative (−0.1 eV) compared to its E_{RHE}. Therefore, the E_{CB} of P-S-T/C was about −0.34 eV (vs RHE). According to eq 6, the valence band energy (E_{VB}) of P-S-T/C was 2.76 eV (vs RHE)

$$E_{VB} = E_{CB} + E_g \tag{6}$$

where E_{VB} is the valence band energy, E_{CB} is the conductor band energy, and E_g is the band-gap energy.[64−67] The valence band position of TiO_2 was positive compared to the standard redox potential of $H_2O/^{\bullet}OH$ (2.2 eV) and $OH^-/^{\bullet}OH$ (1.99 eV), and the conduction band position of TiO_2 was negative compared to the standard redox potential of $O_2/^{\bullet}O_2^-$ (−0.33 eV). Therefore, the photogenerated h^+ and e^- could migrate to the TiO_2 surface to produce reactive active species for photodegradation.

2.4.3. Active Species Analysis. To further investigate the role of membrane components in the photocatalytic process, a series of free radical-trapping experiments were performed at pH = 8.0. BQ, *t*-BuOH, and OA served as scavengers to quench $^{\bullet}O_2^-$, and hydroxyl radicals ($^{\bullet}OH$) and h^+, respectively. The photodegradation rates of RhB after inactivation of $^{\bullet}O_2^-$, $^{\bullet}OH$, and h^+ by P-S-T/C were denoted as v_q ($^{\bullet}O_2^-$), v_q ($^{\bullet}OH$), and v_q (h^+), respectively. Compared with the degradation rate of the membrane without scavengers, the order for the photocatalytic reaction rates was v_q ($^{\bullet}O_2^-$) < v_q ($^{\bullet}OH$) < v_q (h^+) < v (no scavengers) (Figure 11a). The removal rates of RhB by P-S-T/C after inactivating $^{\bullet}O_2^-$, $^{\bullet}OH$,

https://doi.org/10.1021/acsomega.2c00686
ACS Omega 2022, 7, 17128−17143

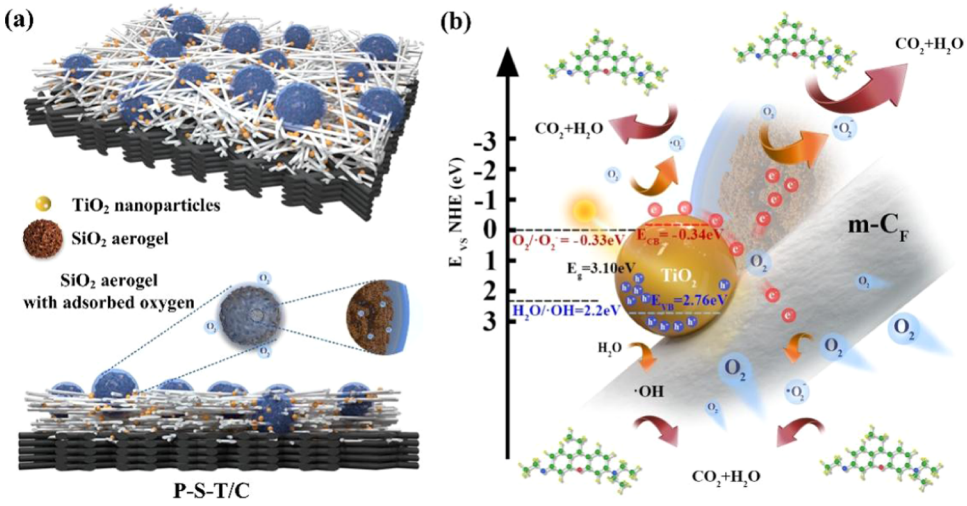

Figure 12. Schematic diagram of the RhB removal mechanism by the P-S-T/C dual-layer composite membrane.

and h^+ were 42.13, 72.92, and 84.99%, respectively. It could be seen that P-S-T/C exhibited the lowest photocatalytic performance after inactivation of $^{\bullet}O_2^-$, indicating that $^{\bullet}O_2^-$ played the predominant role in the photocatalytic process. The elimination of $^{\bullet}OH$ and h^+ inhibited the rate of photocatalytic reaction and the degree of photodegradation for P-S-T/C. $^{\bullet}O_2^-$ was mainly originated from O_2, which acted as an e^- trapping agent to produce $^{\bullet}O_2^-$ and further generated $^{\bullet}OH$ for photodegradation.

The above studies showed that P-TiO_2/C and P-S-T/C had similar adsorption capabilities for RhB, while P-S-T/C with addition of the SiO_2 aerogel showed an improved photodegradation rate for RhB in comparison to P-TiO_2/C. By combining with free radical-trapping experiments, we proposed a reasonable hypothesis that the addition of the SiO_2 aerogel would increase the O_2 contents of the composite membrane, which would bond with the separated e^- to generate $^{\bullet}O_2^-$ via photocatalysis.[68,69] To compare the contents of $^{\bullet}O_2^-$ formed by P-TiO_2/C and P-S-T/C in the process of photodegradation, EPR experiment was conducted in methanol using DMPO as a capture agent. As shown in Figure 11b, the DMPO−$^{\bullet}O_2^-$ signal intensity of P-S-T/C was higher than that of P-TiO_2/C. This result supported the above hypothesis.

The increase of adsorbed O_2 by the SiO_2 aerogel in the composite membrane might result in the decrease of work function of photocatalytic materials. Many studies had shown that photocatalysts with low work function could be regarded as e^- donors and would facilitate escape of e^- from the material's surface, and thus the activity of the reactive species would be promoted.[25,70] The work functions of P-TiO_2/C and P-S-T/C were characterized by UPS, as shown in Figure 11c. The intercepts in the high-binding energy region (17−19 eV) were 17.10 eV for P-TiO_2/C and 17.19 eV for P-S-T/C, respectively. The work functions of P-TiO_2/C and P-S-T/C were 4.11 and 4.02 eV after calculation, respectively. It could be inferred that the addition of the SiO_2 aerogel reduced the work function of the composite materials. This might be due to the abundant O_2 contents of the SiO_2 aerogel with the micro/nano network structure. However, the generation of kinetics of the reactive species on the surface/interface of the materials lacks clarity in the current studies, and the mechanism still needs to be further explored.

The high-resolution XPS O 1s spectra of P-TiO_2/C and P-S-T/C are shown in Figure 11d. The characteristic peaks at 529.3 and 531.4 eV for P-TiO_2/C were attributed to the TiO_2 lattice oxygen and surface hydroxyl groups, respectively. In comparison to P-TiO_2/C, the enhanced and broadened peak of P-S-T/C at 531.4 eV was due to the increased contents of hydroxyl groups on the material's surface upon the addition of the SiO_2 aerogel.[68]

2.4.4. Possible Mechanism of Organic Dye Removal. The mechanism for organic dye removal includes two processes: adsorption and photodegradation.

2.4.4.1. Adsorption. As shown in Figure 12a, the adsorption mechanism was analyzed as follows. The capillary condensation by the architecture of the dual-layer composite membrane endowed P-S-T/C the adsorption capability. Meanwhile, the porous region, which was formed by TiO_2 nanoparticles and the SiO_2 aerogel on the dual-layer composite membrane, provided more adsorption space for organic dyes. The whole process contained two parts: (1) the C_{FC} substrate could adsorb 13.64% of RhB under dark conditions within 30 min. The PVDF/TiO_2 single-layer membrane could barely adsorb RhB. After combining with the C_{FC} substrate, the adsorption rate of the P-TiO_2/C dual-layer composite membrane increased to 20.42%. (2) The addition of the SiO_2 aerogel further improved the adsorption capability of the dual-layer composite photocatalysts. The adsorption capability of P-S-T/C was higher than P-TiO_2/C. It was attributed to the micro/nanoporous structure of the SiO_2 aerogel, which provided more adsorption space for organic dyes. Besides, the surface of the SiO_2 aerogel had a large number of hydroxyl groups, which would form hydrogen bond interactions with the carboxyl groups of RhB.

2.4.4.2. Photocatalytic Degradation. Research work had shown that the photocatalytic process occurred near the adsorption sites.[71,72] In this research, photogenerated e^- was excited from the valence band of TiO_2 and migrated to the conduction band rapidly under simulated sunlight irradiation (eq 7). (1) The valence band position of TiO_2 (2.76 eV) was more positive than the standard redox potential of $H_2O/^{\bullet}OH$ (2.2 eV) and $OH^-/^{\bullet}OH$ (1.99 eV), so the h^+ in the valence band would migrate to the semiconductor surface and convert rich H_2O molecules or surface hydroxyl groups to $^{\bullet}OH$ (eq 8). (2) Photogenerated e^- played the photocatalytic role through

https://doi.org/10.1021/acsomega.2c00686
ACS Omega 2022, 7, 17128−17143

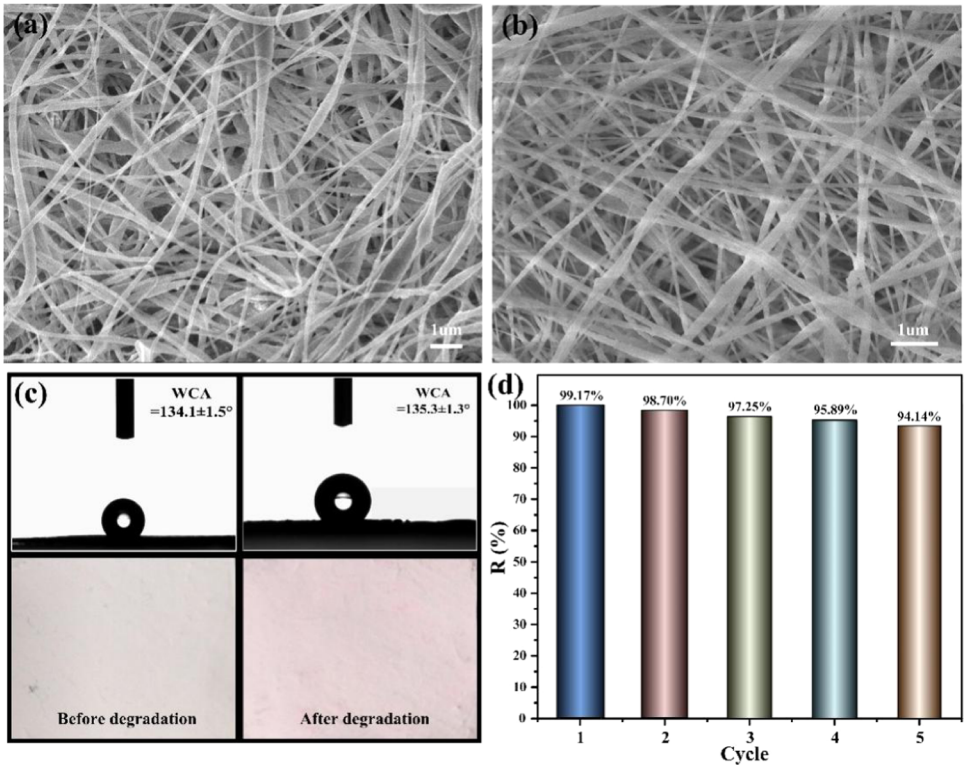

Figure 13. SEM images of P-TiO_2/C (a) and P-S-T/C (b) after degradation. (c) WCA and the photograph of the surface of P-S-T/C before and after photodegradation. (d) Reusability of P-S-T/C for the degradation of RhB [initial concentration = 12 mg L^{-1}, photocatalyst = 0.4 g, pH = 8.0, simulated sunlight irradiation].

two paths. In the first reaction path, the photogenerated e^- separated under simulated sunlight directly reacted with the O_2 molecules in aqueous solution around the TiO_2, and formed $^{\bullet}O_2^-$ (eq 9). This reaction was attributed to the fact that the conduction band position of TiO_2 (−0.34 eV) was more negative than the standard redox potential of $O_2/^{\bullet}O_2^-$ (−0.33 eV). Part of $^{\bullet}O_2^-$ combined with H^+ to form H_2O_2 (eqs 10 and 11), which could be decomposed into $^{\bullet}OH$ (eq 12). The second reaction path was that the photogenerated e^- migrated to the interface of the three-phase heterostructure, and reacted with the adsorbed O_2 molecules to form $^{\bullet}O_2^-$ (eq 9), then further produced $^{\bullet}OH$ (eqs 10−12).[73] These active radicals would degrade the organic pollutant molecules into small molecules, e.g., H_2O and CO_2 (eq 13).

$$TiO_2 + \text{light} \rightarrow h^+ + e^- \quad (7)$$

$$h^+ + H_2O \rightarrow {}^{\bullet}OH + H^+/h^+ + OH^-_{ads} \rightarrow {}^{\bullet}OH \quad (8)$$

$$e^- + O_{2ads} \rightarrow {}^{\bullet}O_2^- \quad (9)$$

$$^{\bullet}O_2^- + H^+ \rightarrow HO_2^{\bullet} \quad (10)$$

$$2HO_2^{\bullet} \rightarrow H_2O_2 + O_2 \quad (11)$$

$$H_2O_2 + e^- \rightarrow {}^{\bullet}OH + OH^- \quad (12)$$

$$h^+/^{\bullet}O_2^-/^{\bullet}OH + \text{RhB} \rightarrow H_2O + CO_2 \quad (13)$$

According to the above analysis, the photocatalytic mechanism could be summarized as follows: (1) the heterostructure coupled by the TiO_2 nanoparticles, SiO_2 aerogel, and C_{FC} substrate accelerated the separation of photogenerated e^-−h^+ pairs and inhibited their recombination; (2) the conductive porous network architecture provided a convenient path for the photogenerated charges' transport;[74] and (3) the addition of the SiO_2 aerogel increased the contents of O_2 and hydroxyl groups on the P-S-T/C surface, which could be used as e^- and h^+ trapping agents, and further accelerated the photocatalytic reaction process. The photodegradation mechanism for P-TiO_2/C is shown in Figure S5, and the photodegradation mechanism for P-S-T/C with the three-phase interface heterostructure is shown in Figure 12b.

2.5. Stability of the Dual-Layer Composite Membrane. The morphologies of P-TiO_2/C and P-S-T/C after degradation for five cycles are shown in Figure 13a,b. Compared to their morphologies before degradation (see Figure 3b,d), no obvious difference was observed. As revealed in Figure 13c, the WCA of P-S-T/C before and after degradation was 134.1 ± 1.5 and 135.3 ± 1.3°, respectively. As shown in Figure 13d, the P-S-T/C still showed high photocatalytic performance under simulated sunlight irradiation after five cycles, which was higher than that of the photocatalysts reported so far.[75,76] All of these indicated that P-S-T/C had excellent cyclic stability.

3. CONCLUSIONS

In this work, an O_2-rich membrane with a three-phase interface heterostructure was prepared. The capillary condensation by architecture of the dual-layer composite membrane endowed its adsorption capability, and the porous region provided more adsorption space for organic dyes. The study of the photodegradation mechanism indicated that the separated photogenerated carriers diffused to the composite membrane surface rapidly on the three-phase interface of P-S-T/C. The abundant O_2 adsorbed on the porous SiO_2 aerogel surface

https://doi.org/10.1021/acsomega.2c00686
ACS Omega 2022, 7, 17128−17143

Scheme 1. Schematic Illustration of the Preparation Process of the Dual-Layer Composite Membrane

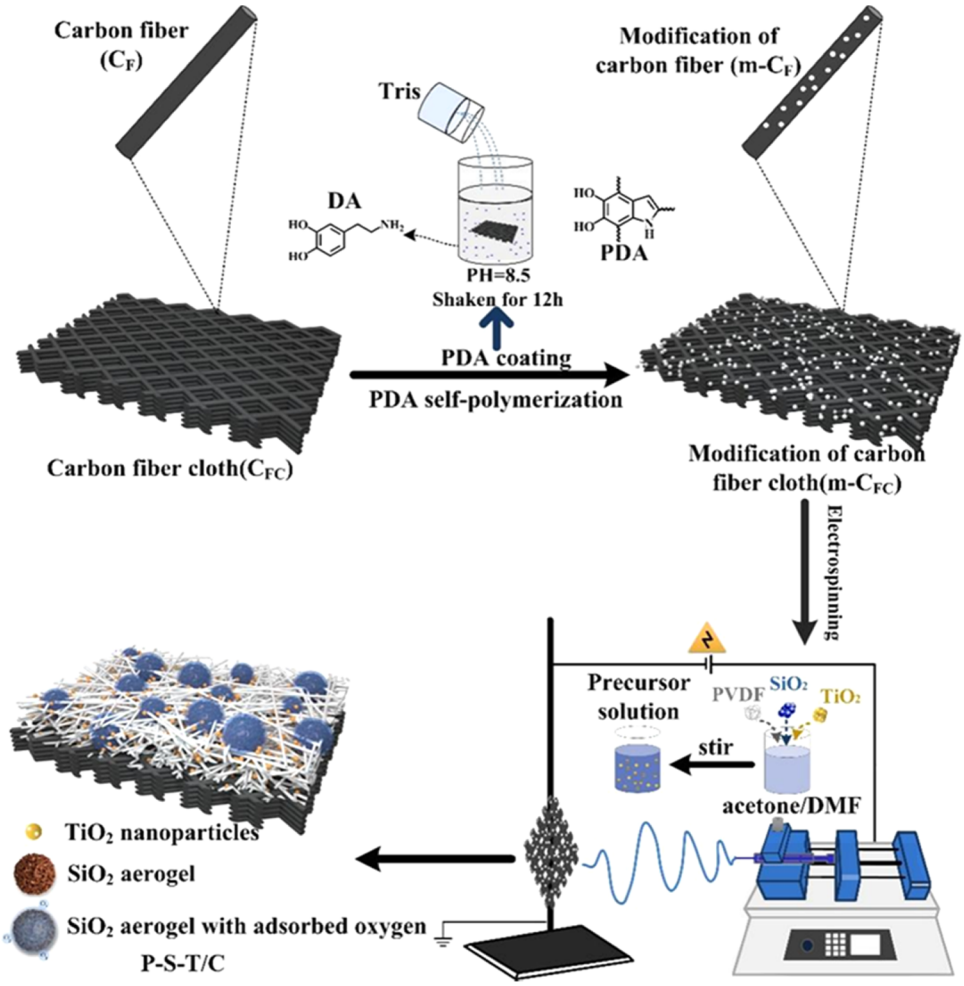

acted as the e^- trapping agent, which could also decrease the work function of the composite materials. The removal rates of P-S-T/C were higher than 99.17% for cationic dyes at pH = 8.0 and higher than 99.99% for the anionic organic dye at pH = 2.0 within 60 min. The P-S-T/C could be used as a universal photocatalyst to remove organic dyes by controlling the pH values. This work established a controlled strategy for optimizing the composite membrane with photocatalytic performance by designing a three-phase heterostructure.

4. EXPERIMENTAL SECTION

4.1. Materials. Anatase phase titanium dioxide (TiO_2) nanoparticles (nanopowder, particle size <25 nm, metal basis), Na_2CO_3 (M_w − 105.99 g/mol), rhodamine B (RhB), methyl orange (MO), methylene blue (MB), dopamine (DA), and Tris(hydroxymethyl)-aminomethane were all purchased from Aladdin Industrial Corporation, Shanghai, China. Hydrophilic silicon dioxide (SiO_2) aerogel (NAF-880, particle size 1−10 μm) was obtained from Xiamen Namet New Material Technology Co. Ltd. Poly(vinylidene fluoride) (PVDF) (Solef 6010, M_w − 600 000 g/mol) was supplied by Solvay Advanced Polymers. *N*,*N*-dimethylformamide (DMF), acetone, hydrochloric acid (HCl, 36−38%), and sodium hydroxide (NaOH) were purchased from Beijing Chemical Works. Conductive carbon fiber cloth (C_{FC}) (HCP330N) was purchased from Shanghai Hesen Electric Co. Ltd. *Tert*-butanol (*t*-BuOH), oxalic acid (OA), and benzoquinone (BQ) were all purchased from Sinopharm Chemical Reagent Co. Ltd. 5,5-Dimethyl-1-pryrroline-N-oxide (DMPO, M_w − 113.16 g/mol, 98%) was purchased from Saen Chemical Technology Co. Ltd. Deionized water was obtained from the laboratory. These chemicals were all of analytical grade and used without further purification.

4.2. Modification of the C_{FC} Substrate. The Tris buffer was gradually added into 400 mL DA solutions (2 mg mL^{-1}) and adjusted to pH 8.5 for DA polymerization at alkaline conditions.[77] Then, the C_{FC} substrate was soaked in the above solutions for 12 h; the modified C_{FC} (m-C_{FC}) substrate was washed with deionized water several times and dried in the oven at 40 °C overnight.

4.3. Modification of the C_{FC} Substrate. The PVDF powder was immersed in a suspension of carbonate buffer (0.5 mg mL^{-1}) and stirred at 55 °C for 12 h. The modified powder was cleaned by deionized water and ethanol three times, subsequently dried in the oven at 40 °C overnight, and the activated PVDF powder was obtained.

10% (w/v) activated PVDF powder was dissolved in an acetone/DMF (3/7, v/v) mixed solution and stirred for 12 h to receive the homogeneous PVDF solution. The different contents of TiO_2 nanoparticles (1, 2, 3, 4%, w/v) were added to the PVDF solutions and stirred for 24 h as the precursor solutions of PVDF/TiO_2. For comparison, 0.1 g of hydrophilic SiO_2 aerogel was dispersed into the PVDF solutions and stirred for 2 h to receive the PVDF/SiO_2 precursor solutions. PVDF/

https://doi.org/10.1021/acsomega.2c00686
ACS Omega 2022, 7, 17128−17143

SiO_2/TiO_2 precursor solutions were prepared by adding 0.1 g of hydrophilic SiO_2 aerogel and TiO_2 nanoparticles (3%, w/v) successively. All electrospinning precursor solutions were ultrasonically processed for 30 min before use.

4.4. Preparation of the Dual-Layer Composite Membrane. The as-prepared dual-layer composite membrane included two parts: the substrate was C_{FC} and the top layer was the electrospun composite nanofibrous membrane. The above precursor solutions were placed into a 5 mL plastic syringe (with an inner diameter of 0.6 mm). The PVDF, PVDF/SiO_2, PVDF/TiO_2, and PVDF/SiO_2/TiO_2 precursor solutions were electrospun on the C_{FC} substrate. The parameter for electrospinning was as follows: the feeding rate of the solutions was 0.5 mL h^{-1}, the applied voltage was 16 kV, and the distance between the tip and the grounded collector was ∼17 cm. The electrospinning process was carried out at 20 ± 2 °C with 10−15% relative humidity. All of the prepared dual-layer composite membranes were dried at room temperature for 24 h to remove the residual organic solvents for further study. The solutions' compositions for different samples are shown in Table S1 and the preparation process of the dual-layer composite membrane is shown in Scheme 1.

4.5. Characterizations. The structures of the C_{FC} substrate before and after modification, and PVDF powder before and after activation in carbonate buffer were characterized by Fourier transform infrared spectroscopy (FTIR, FTIR-4100, JASCO, Japan) in the range of 400−4000 cm^{-1}. The surface morphologies of the top-layer membrane were observed by field emission scanning electron microscopy (FE-SEM, JSM-6700 F, JEOL, Japan). Before SEM examination, all samples were sputtered three times with platinum for 70 s under vacuum conditions. The internal structures and the corresponding elemental mapping of the composite membrane were detected by a transmission electron microscope (TEM, JEM-2100 F, JEOL, Japan). The viscosity and conductivity of the electrospinning precursor solutions were determined by a viscometer (NDJ-1, Yutong, China) and conductivity meter (DDS-11A, Shengci, China). The surface property of the composite membrane was analyzed by laser scanning confocal microcopy (LSCM, 2EXT). The average diameter of the electrospun nanofibers was calculated by ImageJ software. Brunauer−Emmett−Teller (BET, Autosorb-iQ2, Quantachrome Instruments, China) was used to determine the porosity and specific surface areas of the composite membranes. The X-ray photoelectron spectroscope (XPS, ESCALab220i-XL VG Science, Walser M. M.) was used to analyze the surface chemical elements of the composite membrane. The photodegradation test was carried out using a spherical xenon lamp (350 W, XD-300, China) and the absorbance values of the RhB solutions were monitored by UV−vis spectroscopy (UV-6100S, MAPADA, China). The pH of the organic dye solutions was measured by a Pen type pH meter (pH8180-0-00, Hong Kong Xima Instrument Technology Co. Ltd.). Before the pH examination, the pH of the organic dye solutions was adjusted using HCl or NaOH from 2.0 to 8.0, while other conditions remained unchanged. The surface ζ-potential of the membrane was determined by a nanoparticle size and ζ-potential analyzer (NanoZS90, England). UV−vis diffuse reflectance spectroscopy (UV−vis DRS) was done using a Cary 500 spectrometer. The electrochemical properties were investigated by an electrochemical workstation (CHI660D, China). The as-prepared dual-layer composite membrane, a Pt nod, and an Ag/AgCl electrode were used as the working, counter, and reference electrodes, respectively. Electron paramagnetic resonance spectroscopy (EPR) was used to investigate the formation of free radicals during the photocatalytic reaction by using a Bruker EleXsys EPR spectrometer (E500, Germany), and DMPO was used as the spin-trapping agent at room temperature under simulated sunlight. The ultraviolet photoelectronic spectrum (UPS) was used to determine the work function of the composite materials by using pHI5000 VersaProbe III (Scanning ESCA Microprobe) SCA (Spherical Analyzer). The hydrophobic property of the membrane surface was measured by the water contact angle (WCA) with a drop shape analyzer (DSA100, Kruss, Germany).

4.6. Adsorption and Photocatalytic Measurement. The dual-layer composite membrane (0.4 g) was immersed in a 12 mg L^{-1} organic dye solution (60 mL) and stirred in the dark condition for 30 min. Then the mixer was irradiated for 60 min in a beaker under simulated sunlight (350 W), and the intensity of the light was ∼20 mW $(cm^2)^{-1}$. The concentrations of RhB, MB, and MO before and after degradation were obtained at wavelengths of 552, 664, and 463 nm by a UV−vis spectrophotometer, respectively. The removal rates (R %) of organic dyes were calculated as follows

$$R\% = \frac{C_0 - C_t}{C_0} \times 100\% \tag{14}$$

where C_0 (mg L^{-1}) and C_t (mg L^{-1}) represent the initial and equilibrium concentration of the organic dyes, respectively.

■ ASSOCIATED CONTENT

Supporting Information

The Supporting Information is available free of charge at https://pubs.acs.org/doi/10.1021/acsomega.2c00686.

Additional results for the SEM of SiO_2 aerogel; evaluation of photodegradation efficiency of P-TiO_2 under light irradiation and non-light; photodegradation kinetics analysis of P-S-T/C under different pH; photodegradation mechanism of P-TiO_2; solutions compositions of different nanofibers; properties of the electrospinning precursor solutions; element contents in composite membranes; degradation efficiency and kinetic parameters of different samples; comparison of degradation efficiency with other works; BET analysis of composite membranes (PDF)

■ AUTHOR INFORMATION

Corresponding Author

Lili Li − *Key Laboratory of Automobile Materials, Ministry of Education, and College of Materials Science and Engineering, Jilin University, Changchun 130022, China;* orcid.org/0000-0003-2260-2312; Email: lilyllee@jlu.edu.cn

Authors

Li Liu − *Key Laboratory of Automobile Materials, Ministry of Education, and College of Materials Science and Engineering, Jilin University, Changchun 130022, China*

Doudou Wang − *Key Laboratory of Automobile Materials, Ministry of Education, and College of Materials Science and Engineering, Jilin University, Changchun 130022, China*

Jun Huang − *Key Laboratory of Automobile Materials, Ministry of Education, and College of Materials Science and Engineering, Jilin University, Changchun 130022, China*

https://doi.org/10.1021/acsomega.2c00686
ACS Omega 2022, 7, 17128−17143

Zhixuan Huang − *Key Laboratory of Automobile Materials, Ministry of Education, and College of Materials Science and Engineering, Jilin University, Changchun 130022, China*
Ye Zhang − *Key Laboratory of Automobile Materials, Ministry of Education, and College of Materials Science and Engineering, Jilin University, Changchun 130022, China*

Complete contact information is available at:
https://pubs.acs.org/10.1021/acsomega.2c00686

Author Contributions

All authors have given approval to the final version of the manuscript.

Notes

The authors declare no competing financial interest.

■ ACKNOWLEDGMENTS

This research was supported by the Natural Science Foundation of Jilin Province, China (No. 20210101051JC) and the Key Laboratory of Polymer Ecomaterials, Changchun Institute of Applied Chemistry, Chinese Academy of Sciences, Open Project (20201201).

■ ABBREVIATIONS

e^-, electron; h^+, hole; $^{\bullet}O_2^-$, superoxide radicals; $^{\bullet}OH$, hydroxyl radicals; C_{FC}, carbon fiber cloth; m-C_{FC}, modified carbon fiber cloth; TiO_2, titanium dioxide; SiO_2, silicon dioxide; O_2, oxygen; N_2, nitrogen; PVDF, poly(vinylidene fluoride); DA, dopamine; PDA, polydopamine; RhB, rhodamine B; MO, methyl orange; MB, methylene blue; DMF, *N*,*N*-dimethylformamide; HCl, hydrochloric acid; NaOH, sodium hydroxide; *t*-BuOH, *tert*-butanol; OA, oxalic acid; BQ, benzoquinone; DMPO, 5,5-dimethyl-1-pryrroline-N-oxide; *R*%, removal rate; RMS, root-mean-square; R^2, determined coefficient; E_{fb}, potential value; E_{CB}, conduction band energy; E_{VB}, valence band energy

■ REFERENCES

(1) Li, B. R.; Meng, M. J.; Cui, Y. H.; Wu, Y. L.; Zhang, Y. L.; Dong, H. J.; Zhu, Z.; Feng, Y. H.; Wu, C. D. Changing Conventional Blending Photocatalytic Membranes (BPMs): Focus on Improving Photocatalytic Performance of Fe_3O_4/g-C_3N_4/PVDF Membranes through Magnetically Induced Freezing Casting Method. *Chem. Eng. J.* **2019**, *365*, 405−414.
(2) Zhou, Y. B.; Lu, J.; Zhou, Y.; Liu, Y. D. Recent Advances for Dyes Removal Using Novel Adsorbents: A Review. *Environ. Pollut.* **2019**, *252*, 352−365.
(3) Wang, M. Y.; Ioccozia, J.; Sun, L.; Lin, C. J.; Lin, J. Q. Inorganic-Modified Semiconductor TiO_2 Nanotube Arrays for Photocatalysis. *Energy Environ. Sci.* **2017**, *10*, 2041.
(4) Zhu, M. X.; Lee, L.; Wang, H. H.; Wang, Z. Removal of an Anionic Dye by Adsorption/Precipitation Processes Using Alkaline White Mud. *J. Hazard. Mater.* **2007**, *149*, 735−741.
(5) Dhakshinamoorthy, A.; Navalon, S.; Corma, A.; Garcia, H. Photocatalytic CO_2 Reduction by TiO_2 and Related Titanium Containing Solids. *Energy Environ. Sci.* **2012**, *5*, 9217−9233.
(6) Wang, Y.; Wang, S. B.; Lou, X. W. Dispersed Nickel Cobalt Oxyphosphide Nanoparticles Confined in Multichannel Hollow Carbon Fibers for Photocatalytic CO_2 Reduction. *Angew. Chem., Int. Ed.* **2019**, *58*, 17236−17240.
(7) Yu, J. G.; Jin, J.; Cheng, B.; Jaroniec, M. A Noble Metal-Free Reduced Graphene Oxide-CdS Nanorod Composite for the Enhanced Visible-Light Photocatalytic Reduction of CO_2 to Solar Fuel. *J. Mater. Chem. A* **2014**, *2*, 3407−3416.
(8) Huang, T. B.; Xu, Z. X.; Zeng, G. C.; Zhang, P. Y.; Song, T.; Wang, Y. L.; Wang, T.; Huang, S. B.; Wang, T. T.; Zeng, H. P. Selective Deposition of Plasmonic Copper on Few Layers Graphene with Specific Defects for Efficiently Synchronous Photocatalytic Hydrogen Production. *Carbon* **2019**, *143*, 257−267.
(9) Li, F. X.; Xiao, X. D.; Zhao, C.; Liu, J. N.; Li, Q.; Guo, C. Y.; Tian, C. G.; Zhang, L. P.; Hu, J. A.; Jiang, B. J. TiO_2-on-C_3N_4 Double-Shell Microtubes: In-Situ Fabricated Heterostructures toward Enhanced Photocatalytic Hydrogen Evolution. *J. Colloid Interface Sci.* **2020**, *572*, 22−30.
(10) Khalily, M. A.; Yurderi, M.; Haider, A.; Bulut, A.; Patil, B.; Zahmakiran, M.; Uyar, T. Atomic Layer Deposition of Ruthenium Nanoparticles on Electrospun Carbon Nanofibers: Highly Efficient Nanocatalyst for the Hydrolytic Dehydrogenation of Methylamine-Borane. *ACS Appl. Mater. Interfaces* **2018**, *10*, 26162−26169.
(11) Lan, J.; Wang, Y.; Huang, B.; Xiao, Z. C.; Wu, P. F. Application of Polyoxometalates in Photocatalytic Degradation of Organic Pollutants. *Nanoscale Adv.* **2021**, *3*, 4646−4658.
(12) Kong, L. S.; Dong, N. X.; Qi, S. L.; Tian, G. F.; Wu, D. Z. Facile Fabrication of Size-Controlled Ag@PI Hybrid Nanotubes and Its Photocatalytic Performance. *Mater. Lett.* **2020**, *277*, No. 128374.
(13) Binding, D.; Steinbach, F. Homogeneous Photocatalysis by Organic Dyes in the Liquid Phase. *Nature* **1970**, *227*, 832−833.
(14) Kampouri, S.; Nguyen, T. N.; Spodaryk, M.; Palgrave, R. G.; Züttel, A.; Smit, B.; Stylianou, K. C. Concurrent Photocatalytic Hydrogen Generation and Dye Degradation Using MIL-125-NH_2 under Visible Light Irradiation. *Adv. Funct. Mater.* **2018**, *28*, No. 1806368.
(15) Shi, H. M.; Zhang, S.; Zhu, X. P.; Liu, Y.; Wang, T.; Jiang, T.; Zhang, G. H.; Duan, H. G. Uniform Gold-Nanoparticle-Decorated {001}-Faceted Anatase TiO_2 Nanosheets for Enhanced Solar-Light Photocatalytic Reactions. *ACS Appl. Mater. Interfaces* **2017**, *9*, 36907−36916.
(16) Selli, E. Synergistic Effects of Sonolysis Combined with Photocatalysis in the Degradation of an Azo Dye. *Phys. Chem. Chem. Phys.* **2002**, *4*, 6123−6128.
(17) Guo, Q.; Zhou, C. Y.; Ma, Z. B.; Yang, X. M. Fundamentals of TiO_2 Photocatalysis: Concepts, Mechanisms, and Challenges. *Adv. Mater.* **2019**, *31*, No. 1901997.
(18) Yu, X.; Jin, X.; Chen, X. Y.; Wang, A. Z.; Zhang, J. M.; Zhang, J.; Zhao, Z. H.; Gao, M. M.; Razzari, L.; Liu, H. A Microorganism Bred TiO_2/Au/TiO_2 Heterostructure for Whispering Gallery Mode Resonance Assisted Plasmonic Photocatalysis. *ACS Nano* **2020**, *14*, 13876.
(19) Fei, J. B.; Li, J. B. Controlled Preparation of Porous TiO_2-Ag Nanostructures through Supramolecular Assembly for Plasmon-Enhanced Photocatalysis. *Adv. Mater.* **2015**, *27*, 314−319.
(20) Chatterjee, D.; Dasgupta, S.; Rao, N. N. Visible Light Assisted Photodegradation of Halocarbons on the Dye Modified TiO_2 Surface Using Visible Light. *Sol. Energy Mater. Sol. Cells* **2006**, *90*, 1013−1020.
(21) Chandrasekaran, S.; Bowen, C.; Zhang, P. X.; Li, Z. L.; Yuan, Q. H.; Ren, X. Z.; Deng, L. B. Spinel Photocatalysts for Environmental Remediation, Hydrogen Generation, CO_2 Reduction and Photoelectrochemical Water Splitting. *J. Mater. Chem. A* **2018**, *6*, 11078−11104.
(22) Meng, A. Y.; Wu, S.; Cheng, B.; Yu, J. G.; Xu, J. S. Hierarchical TiO_2/$Ni(OH)_2$ Composite Fibers with Enhanced Photocatalytic CO_2 Reduction Performance. *J. Mater. Chem. A* **2018**, *6*, 4729−4736.
(23) Yu, Y. T.; Xu, W. C.; Fang, J. Z.; Chen, D. D.; Pan, T.; Feng, W. H.; Liang, Y.; Fang, Z. Q. Soft-Template Assisted Construction of Superstructure TiO_2/SiO_2/g-C_3N_4 Hybrid as Efficient Visible-Light Photocatalysts to Degrade Berberine in Seawater via an Adsorption-Photocatalysis Synergy and Mechanism Insight. *Appl. Catal., B* **2020**, *268*, No. 118751.
(24) Xiao, J.; Yang, W. Y.; Li, Q. Bi Quantum Dots on Rutile TiO_2 as Hole Trapping Centers for Efficient Photocatalytic Bromate Reduction under Visible Light Illumination. *Appl. Catal., B* **2017**, *218*, 111−118.

(25) Lee, S. Y.; Kim, U. J.; Chung, J. G.; Nam, H. G.; Jeong, H. Y.; Han, G. H.; Kim, H.; Oh, H. M.; Lee, H.; Kim, H.; Roh, Y. G.; Kim, j.; Hwang, S. W.; Park, Y.; Lee, Y. H. Large Work Function Modulation of Monolayer MoS_2 by Ambient Gases. *ACS Nano* **2016**, *10*, 6100−6107.
(26) Liu, Y. P.; Li, Y. H.; Li, X. Y.; Zhang, Q.; Yu, H.; Peng, X. W.; Peng, F. Regulating Electron-Hole Separation to Promote Photocatalytic H_2 Evolution Activity of Nanoconfined Ru/MXene/TiO_2 Catalysts. *ACS Nano* **2020**, *14*, 14181−14189.
(27) Yu, H. L.; Wu, Q. X.; Wang, J.; Liu, L. Q.; Zheng, B.; Zhang, C.; Shen, Y. G.; Huang, C. L.; Zhou, B.; Jia, J. R. Simple Fabrication of the Ag-Ag_2O-TiO_2 Photocatalyst Thin Films on Polyester Fabrics by Magnetron Sputtering and Its Photocatalytic Activity. *Appl. Surf. Sci.* **2020**, *503*, No. 144075.
(28) Chen, H. R.; Shen, K.; Chen, J. Y.; Chen, X. D.; Li, Y. W. Hollow-ZIF-Templated Formation of a ZnO@C-N-Co Core-Shell Nanostructure for Highly Efficient Pollutant Photodegradation. *J. Mater. Chem. A* **2017**, *5*, 9937−9945.
(29) Wang, X. T.; Zhou, J. Q.; Zhao, S.; Chen, X.; Yu, Y. Synergistic Effect of Adsorption and Visible-Light Photocatalysis for Organic Pollutant Removal over $BiVO_4$/Carbon Sphere Nanocomposites. *Appl. Surf. Sci.* **2018**, *453*, 394−404.
(30) Lee, H.; Dellatore, S. M.; Miller, W. M.; Messersmith, P. B. Mussel-Inspired Surface Chemistry for Multifunctional Coatings. *Science* **2007**, *318*, 426−430.
(31) Liu, R.; Dai, L.; Si, C. L. Mussel-Inspired Cellulose-Based Nanocomposite Fibers for Adsorption and Photocatalytic Degradation. *ACS Sustainable Chem. Eng.* **2018**, *6*, 15756−15763.
(32) Chen, S. Y.; Liu, S.; Zhang, L. L.; Han, Q.; Liu, H. Q.; Shen, J. H.; Li, G. C.; Zhang, L. Z.; Yang, Y. M. Construction of Injectable Silk Fibroin/Polydopamine Hydrogel for Treatment of Spinal Cord Injury. *Chem. Eng. J.* **2020**, *399*, No. 125795.
(33) Farooq, U.; Zhuang, J. G.; Wang, X. H.; Lyu, S. G. A Recyclable Polydopamine-Functionalized Reduced Graphene Oxide/Fe Nanocomposite (PDA@Fe/rGO) for the Enhanced Degradation of 1,1,1-Trichloroethane. *Chem. Eng. J.* **2021**, *403*, No. 126405.
(34) Liu, S. Y.; Wang, J. T. Eco-Friendly and Facile Fabrication of Polyimide Mesh with Underwater Superoleophobicity for Oil/Water Separation via Polydopamine/Starch Hybrid Decoration. *Sep. Purif. Technol.* **2020**, *250*, No. 117228.
(35) Saha, D.; Hoinkis, T. J.; Van Bramer, S. E. Electrospun, Flexible and Reusable Nanofiber Mat of Graphitic Carbon Nitride: Photocatalytic Reduction of Hexavalent Chromium. *J. Colloid Interface Sci.* **2020**, *575*, 433−442.
(36) Cai, K.; Hang, X.; Zhao, Y.; Zong, R. L.; Zeng, F.; Guo, D. A Green Route to a Low Cost Anisotropic MoS_2/Poly (Vinylidene Fluoride) Nanocomposite with Ultrahigh Electroactive Phase and Improved Electrical and Mechanical Properties. *ACS Sustainable Chem. Eng.* **2018**, *6*, 5043−5052.
(37) Wei, Y. X.; Zhang, D. Z.; Liu, Z. M.; Su, B. L. Highly Efficient Catalytic Conversion of Chloromethane to Light Olefins over HSAPO-34 as Studied by Catalytic Testing and in Situ FTIR. *J. Catal.* **2006**, *238*, 46−57.
(38) Tan, W. L.; Tan, H. F.; Ahmad, N. A.; Hamzah, N.; Ahmad, A. L.; Leo, C. P. Carbon Capture by Alkaline Absorbent Using Octadecyltrichlorosilane Modified PVDF/TiO_2 Membrane. *Korean J. Chem. Eng.* **2020**, *37*, 505−512.
(39) Kuo, C. H.; Chen, G. J.; Twu, Y. K.; Liu, Y. C.; Shieh, C. J. Optimum Lipase Immobilized on Diamine-Grafted PVDF Membrane and Its Characterization. *Ind. Eng. Chem. Res.* **2012**, *51*, 5141−5147.
(40) Kolesnyk, I.; Kujawa, J.; Bubela, H.; Konovalova, V.; Burban, A.; Cyganiukb, A.; Kujawskib, W. Photocatalytic Properties of PVDF Membranes Modified with g-C_3N_4 in the Process of Rhodamines Decomposition. *Sep. Purif. Technol.* **2020**, *250*, No. 117231.
(41) Ross, G. J.; Watts, J. F.; Hill, M. P.; Morrissey, P. Surface Modification of Poly (Vinylidene Fluoride) by Alkaline Treatment Part 2. Process Modification by the Use of Phase Transfer Catalysts. *Polymer* **2001**, *42*, 403−413.
(42) Vitola, G.; Mazzei, R.; Fontananova, E.; Giorno, L. PVDF Membrane Biofunctionalization by Chemical Grafting. *J. Membr. Sci.* **2015**, *476*, 483−489.
(43) Dobrovolskaya, I. P.; Yudin, V. E.; Popryadukhin, P. V.; Ivan'kova, E. M.; Shabunin, A. S.; Kasatkinc, I. A.; Morgantied, P. Effect of Chitin Nanofibrils on Electrospinning of Chitosan-Based Composite Nanofibers. *Carbohydr. Polym.* **2018**, *194*, 260−266.
(44) Huang, Z. M.; Zhang, Y. Z.; Kotaki, M.; Ramakrishna, S. A Rreview on Polymer Nanofibers by Electrospinning and Their Applications in Nanocomposites. *Compos. Sci. Technol.* **2003**, *63*, 2223−2253.
(45) Okpalugo, T. I. T.; Papakonstantinou, P.; Murphy, H.; McLaughlin, J.; Brown, N. M. D. High Resolution XPS Characterization of Chemical Functionalised MWCNTs and SWCNTs. *Carbon* **2005**, *43*, 153−161.
(46) Hu, L. X.; Zhang, Y. Y.; Lu, W. C.; Lu, Y. S.; Hu, H. M. Easily Recyclable Photocatalyst Bi_2WO_6/MOF/PVDF Composite Film for Efficient Degradation of Aqueous Refractory Organic Pollutants under Visible-Light Irradiation. *J. Mater. Sci.* **2019**, *54*, 6238−6257.
(47) Su, D.; Pei, Y.; Liu, L.; Liu, Z. X.; Liu, J. F.; Yang, M.; Wen, J. X.; Dai, J.; Deng, H. Q.; Cao, G. Z. Wire-in-Wire TiO_2/C Nanofibers Free-Standing Anodes for Li-Ion and K-Ion Batteries with Long Cycling Stability and High Capacity. *Nano−Micro Lett.* **2021**, *13*, No. 107.
(48) Parale, V. G.; Kim, T.; Phadtare, V. D.; Yadav, H. M.; Park, H. H. Enhanced Photocatalytic Activity of a Mesoporous TiO_2 Aerogel Decorated onto Three-Dimensional Carbon Foam. *J. Mol. Liq.* **2019**, *277*, 424−433.
(49) He, S.; Sun, G. X.; Cheng, X. D.; Dai, H. M.; Chen, X. F. Nanoporous SiO_2 Grafted Aramid Fibers with Low Thermal Conductivity. *Compos. Sci. Technol.* **2017**, *146*, 91−98.
(50) Maharjan, B.; Kaliannagounder, V. K.; Jang, S. R.; Awasthi, G. P.; Bhattarai, D. P.; Choukrani, G.; Parka, C. H.; Kim, C. S. In-Situ Polymerized Polypyrrole Nanoparticles Immobilized Poly(Epsilon-Caprolactone) Electrospun Conductive Scaffolds for Bone Tissue Engineering. *Mater. Sci. Eng. C* **2020**, *114*, No. 111056.
(51) Uyguner, C. S.; Miray, B. Application of Photocatalysis for the Removal of Natural Organic Matter in Simulated Surface and Ground Waters. *J. Adv. Oxid. Technol.* **2009**, *12*, 87−92.
(52) Kulterer, M. R.; Reichel, V. E.; Kargl, R.; Köstler, S.; Sarbova, V.; Heinze, T.; Stana-Kleinschek, K.; Ribitsch, V. Functional Polysaccharide Composite Nanoparticles from Cellulose Acetate and Potential Applications. *Adv. Funct. Mater.* **2012**, *22*, 1749−1758.
(53) Zhang, J.; Yan, S.; Fu, L.; Wang, F.; Yuan, M. Q.; Luo, G. X.; Xu, Q.; Wang, X.; Li, C. Photocatalytic Degradation of Rhodamine B on Anatase, Rutile, and Brookite TiO_2. *Chin. J. Catal.* **2011**, *32*, 983−991.
(54) Yao, Y.; Li, K.; Chen, S.; Jia, J. P.; Wang, Y. L.; Wang, H. W. Decolorization of Rhodamine B in a Thin-Film Photoelectrocatalytic (PEC) Reactor with Slant-Placed TiO_2 Nanotubes Electrode. *Chem. Eng. J.* **2012**, *187*, 29−35.
(55) Sher Shah, M. S. A.; Park, A. R.; Zhang, K.; Park, J. H.; Yoo, P. J. Green Synthesis of Biphasic TiO_2-Reduced Graphene Oxide Nanocomposites with Highly Enhanced Photocatalytic Activity. *ACS Appl. Mater. Interfaces* **2012**, *4*, 3893−3901.
(56) Tettey, K. E.; Yee, M. Q.; Lee, D. Photocatalytic and Conductive MWCNT/TiO_2 Nanocomposite Thin Films. *ACS Appl. Mater. Interfaces* **2010**, *2*, 2646−2652.
(57) Li, C. P.; Wang, J. Q.; Feng, S. Q.; Yang, Z. L.; Ding, S. J. Low-Temperature Synthesis of Heterogeneous Crystalline TiO_2-Halloysite Nanotubes and Their Visible Light Photocatalytic Activity. *J. Mater. Chem. A* **2013**, *1*, 8045−8054.
(58) Cao, N. W.; Gu, M. Z.; Gao, M. M.; Li, C.; Liu, K. N.; Zhao, X. Y.; Feng, J.; Ren, Y. M.; Wei, T. A Three-Layer Photocatalyst Carbon Fibers/TiO_2 Seed/TiO_2 Nanorods with High Photocatalytic Degradation under Visible Light. *Appl. Surf. Sci.* **2020**, *530*, No. 147289.
(59) Li, J. N.; Zhang, Q. C.; Liu, J. M.; Yu, M. R.; Ma, H. Y.; Yang, J. C.; Ye, S.; Reina, T. R.; Liu, J. In-Situ Formation of Carboxylate

https://doi.org/10.1021/acsomega.2c00686
ACS Omega 2022, 7, 17128−17143

Species on TiO_2 Nanosheets for Enhanced Visible-Light Photocatalytic Performance. *J. Colloid Interface Sci.* **2020**, *577*, 512−522.
(60) Alaounia, N.; Ouchefoun, M.; Touam, T. Sol-Gel Synthesis of Nanocrystalline TiO_2 and the Investigation of Its Photocatalytic Activity for Degradation of Methyl Orange. *J. New Technol. Mater.* **2021**, *11*, 19−23.
(61) Adebayo, B. O.; Newport, K.; Yu, H.; Rownaghi, A. A.; Liang, X. H.; Rezaei, F. Atomic Layer Deposited Ni/ZrO_2-SiO_2 for Combined Capture and Oxidation of VOCs. *ACS Appl. Mater. Interfaces* **2020**, *12*, 39318−39334.
(62) Lv, K.; Xiang, Q. J.; Yu, J. G. Effect of Calcination Temperature on Morphology and Photocatalytic Activity of Anatase TiO_2 Nanosheets with Exposed {001} Facets. *Appl. Catal., B* **2011**, *104*, 275−281.
(63) Yu, J. G.; Xiang, Q. J.; Zhou, M. H. Preparation, Characterization and Visible-Light-Driven Photocatalytic Activity of Fe-Doped Titania Nanorods and First-Principles Study for Electronic Structures. *Appl. Catal., B* **2009**, *90*, 595−602.
(64) Wang, L.; Lee, C. Y.; Schmuki, P. Solar Water Splitting: Preserving the Beneficial Small Feature Size in Porous Alpha-Fe_2O_3 Photoelectrodes During Annealing. *J. Mater. Chem. A* **2013**, *1*, 212−215.
(65) Saito, R.; Miseki, Y.; Sayama, K. Highly Efficient Photoelectrochemical Water Splitting Using a Thin Film Photoanode of $BiVO_4/SnO_2/WO_3$ Multi-Composite in a Carbonate Electrolyte. *Chem. Commun.* **2012**, *48*, 3833−3835.
(66) Yang, Y. J.; Bian, Z. Y. Oxygen Doping through Oxidation Causes the Main Active Substance in g-C_3N_4 Photocatalysis to Change Form Holes to Singlet Oxygen. *Sci. Total Environ.* **2021**, *753*, No. 141908.
(67) Sun, M.; Yan, T.; Zhang, Y.; He, Y. H.; Shao, Y.; Wei, Q.; Du, B. Rod-Like Bi_4O_7 Decorated $Bi_2O_2CO_3$ Plates: Facile Synthesis, Promoted Charge Separation, and Highly Efficient Photocatalytic Degradation of Organic Contaminants. *J. Colloid Interface Sci.* **2018**, *514*, 240−249.
(68) Benz, D.; Bui, H. V.; Hintzen, H. T.; Kreutzer, M. T.; van Ommen, J. R. Synthesis of a Rationally Designed Multi-Component Photocatalyst Pt:SiO_2:TiO_2(P25) with Improved Activity for Dye Degradation by Atomic Layer Deposition. *Nanomaterials* **2020**, *10*, No. 1496.
(69) Benz, D.; Felter, K. M.; Köser, J.; Thöming, J.; Mul, G.; Grozema, F. C.; Hintzen, H. T.; Kreutzer, M. T.; van Ommen, J. R. Assessing the Role of Pt Clusters on TiO_2 (P25) on the Photocatalytic Degradation of Acid Blue 9 and Rhodamine B. *J. Phys. Chem. C* **2020**, *124*, 8269−8278.
(70) Huang, W. C.; Gao, Y.; Wang, J. X.; Ding, P. C.; Yan, M.; Wu, F. M.; Liu, J.; Liu, D. Q.; Guo, C. S.; Yang, B.; Cao, W. W. Plasmonic Enhanced Reactive Oxygen Species Activation on Low-Work-Function Tungsten Nitride for Direct Near-Infrared Driven Photocatalysis. *Small* **2020**, *16*, No. 2004557.
(71) Sun, Y. Y.; Li, G. H.; Gong, Y.; Sun, Z. F.; Yao, H. L.; Zhou, X. X. Ag and TiO_2 Nanoparticles Co-Modified Defective Zeolite TS-1 for Improved Photocatalytic CO_2 Reduction. *J. Hazard. Mater.* **2021**, *403*, No. 124019.
(72) Wu, X. Q.; Shao, Z. D.; Liu, Q.; Xie, Z. L.; Zhao, F.; Zheng, Y. M. Flexible and Porous TiO_2/SiO_2/Carbon Composite Electrospun Nanofiber Mat with Enhanced Interfacial Charge Separation for Photocatalytic Degradation of Oganic Pollutants in Water. *J. Colloid Interface Sci.* **2019**, *553*, 156−166.
(73) Fakharian-Qomi, M. J.; Sadeghzadeh-Attar, A. Template Based Synthesis of Plasmonic Ag-Modified TiO_2/SnO_2 Nanotubes with Enhanced Photostability for Efficient Visible-Light Photocatalytic H_2 Evolution and RhB Degradation. *ChemistrySelect* **2020**, *5*, 6001−6010.
(74) Mittal, H.; Khanuja, M. Hydrothermal in-Situ Synthesis of $MoSe_2$-Polypyrrole Nanocomposite for Efficient Photocatalytic Degradation of Dyes under Dark and Visible Light Irradiation. *Sep. Purif. Technol.* **2021**, *254*, No. 117508.
(75) Le, T. T.; Le, T. H. T.; Van, K. N.; Bui, H. V.; Le, T. G.; Vo, V. Controlled Growth of TiO_2 Nanoparticles on Graphene by Hydrothermal Method for Visible-Light Photocatalysis. *J. Sci.: Adv. Mater. Devices* **2021**, *6*, 516−527.
(76) Li, Z.; He, Z. J.; Lai, H. J.; He, Y.; Zhu, Z. F.; Chen, Y. F.; Jin, T. One-Step Synthesis of Oxygen-Defects Modified Ta_2O_5 Nanosheets with High Photocatalytic Performance by Chemical Vapor Deposition Method. *Appl. Surf. Sci.* **2021**, *567*, No. 150776.
(77) Shi, S.; Wang, L. B.; Su, R. X.; Liu, B. S.; Huang, R. L.; Qi, W.; He, Z. M. A Polydopamine-Modified Optical Fiber SPR Biosensor Using Electro-Less-Plated Gold Films for Immunoassays. *Biosens. Bioelectron.* **2015**, *74*, 454−460.

https://doi.org/10.1021/acsomega.2c00686
ACS Omega 2022, 7, 17128−17143